



Mapping the Filamentary Nebula of NGC 1275 with Multiwavelength SITELLE Observations

Carter Lee Rhea^{1,2,3} , Julie Hlavacek-Larrondo¹ , Marie-Lou Gendron-Marsolais^{4,5} , Benjamin Vigneron¹ , Megan Donahue⁶ , Auriane Thilloy¹ , Laurie Rousseau-Nepton^{7,8,9} , Mar Mezcua^{10,11} , Norbert Werner¹² , Jorge Barrera-Ballesteros¹³ , Hyunseop Choi^{1,14} , Alastair Edge¹⁵ , Andrew Fabian¹⁶ , and G. Mark Voit⁶

¹Département de physique, Université de Montréal, Succ. Centre-Ville, Montréal, Québec, H3C 3J7, Canada

²Centre de recherche en astrophysique du Québec (CRAQ), Canada

³Dragonfly Focused Research Organization, 150 Washington Avenue, Santa Fe, NM 87501, USA

⁴Instituto de Astrofísica de Andalucía, IAA-CSIC, Apartado 3004, 18080 Granada, España, Spain

⁵Département de physique, de génie physique et d'optique, Université Laval, Québec (QC), G1V 0A6, Canada

⁶Department of Physics and Astronomy, Michigan State University, East Lansing, MI 48824, USA

⁷Canada-France-Hawaii Telescope, 65-1238 Mamalahoa Highway, Kamuela, HI 96743, USA

⁸David A. Dunlap Department of Astronomy & Astrophysics, University of Toronto, 50 St George Street, Toronto, ON M5S 3H4, Canada

⁹Dunlap Institute for Astronomy & Astrophysics, University of Toronto, 50 St George Street, Toronto, ON M5S 3H4, Canada

¹⁰Institute of Space Sciences (ICE, CSIC), Campus UAB, Carrer de Magrans, 08193 Barcelona, Spain

¹¹Institut d'Estudis Espacials de Catalunya (IEEC), Edifici RDIT, Campus UPC, 08860 Castelldefels (Barcelona), Spain

¹²Department of Theoretical Physics and Astrophysics, Faculty of Science, Masaryk University, Kotlářská 2, Brno, 611 37, Czech Republic

¹³Universidad Nacional Autónoma de México, Instituto de Astronomía, AP 70-264, CDMX 04510, Mexico

¹⁴Mila-Quebec Artificial Intelligence Institute, Montreal, Quebec, Canada

¹⁵Centre for Extragalactic Astronomy, Department of Physics, Durham University, South Road, Durham DH1 3LE, UK

¹⁶Institute of Astronomy, Madingley Road, Cambridge CB3 0HA, UK

Received 2024 August 31; revised 2025 February 7; accepted 2025 February 10; published 2025 March 12

Abstract

The filamentary nebula encompassing the central galaxy of the Perseus Cluster, NGC 1275, is a complex structure extending dozens of kiloparsecs from NGC 1275. Decades of previous works have focused on establishing the primary formation and ionization mechanisms in different filaments. These studies have pointed to a lack of star formation in the majority of the filaments, the importance of magnetic fields and turbulence in several regions, and the role of interactions between the intracluster medium (ICM) and the cool gas in the filaments, as well as the role of interaction between the central radio source, 3C84, and the filaments. In this paper, we present multi-filter observations of the entire filamentary system that cover the optical bandpass, using the SITELLE instrument at the Canada-France-Hawai'i Telescope. Here, we use the data analysis software, LUCI (<https://crhea93.github.io/LUCI/index.html>), to produce flux maps of the prominent emission lines present in the filters: [O II] λ 3726/3729, [O III] λ 5007, H β , [N II] λ 6548, [N II] λ 6583, and H α . We use these maps to produce Baldwin–Phillips–Terlevich and WHAN diagrams to study the ionization mechanisms at play in each distinct region of the filamentary nebula. First, we confirm the absence of [O III] λ 5007 in the extended filaments, although we detect this line in the central core, revealing a compact region where photoionization by the active galactic nucleus might affect local conditions. Our findings corroborate previous claims that the ionization in the extended filaments could be caused by the cooling ICM via collisional excitation and/or mixing. Moreover, they support the conclusion that magnetic fields play an important role in the formation and continued existence of the filaments.

Unified Astronomy Thesaurus concepts: Galaxies (573); Galactic and extragalactic astronomy (563); Galaxy spectroscopy (2171)

1. Introduction

Recent observational campaigns targeting nearby galaxies have revealed the presence of a diffuse halo of gas surrounding their host galaxies known as the circumgalactic medium (CGM; see J. Suresh et al. 2015; J. Tumlinson et al. 2017 and P. Barai et al. 2013 for details). The CGM contains the majority of baryons in the galactic system and is thus of vital importance in our understanding of galaxy evolution (e.g., J. N. Bregman et al. 2018; J.-P. Macquart et al. 2020). However, due to the diffuse nature of the gas, the CGM is only detectable in systems with rare extremely deep observations or

those that fortuitously have an illuminating background source (e.g., C. C. Steidel et al. 2010; G. Zhu & B. Ménard 2013).

Despite the fact that the CGM is difficult to study in the majority of galaxies with contemporary observatories, extremely massive galaxies are expected to have very large reservoirs of this diffuse gas. These massive galaxies live in the center of galaxy clusters (≥ 100 galaxies) and have been shown to host a denser, though still diffuse, halo of gas known as the intracluster medium (ICM), which acts as an excellent analog to the CGM of individual galaxies. Indeed, observations have demonstrated that the relative abundances of baryonic matter in the form of stars and gas in addition to dark matter in the ICM are consistent with those of the CGM (e.g., D. P. Marrone et al. 2012). Therefore, studying the ICM, readily detectable with current instruments, is a good starting point in order to glean properties of the CGM.

Multiwavelength observations of the ICM around the nearest and brightest galaxy clusters have revealed that the ICM is highly multiphase (R. Minkowski 1959), spanning several orders of magnitude in temperature and density. Therefore, it can be detected in the X-rays through the highly ionized hot ICM (10^{7-8} K), $H\alpha$ (10^4 K) and/or in the infrared (~ 30 K). Moreover, certain nebulae have been shown to host thread-like filaments stretching over several kiloparsecs (e.g., A. C. Fabian et al. 2008; M. McDonald et al. 2011).

The origin of the multiphase gas in the ICM is still unknown. Although optical emission of this type is associated with star formation, there is little evidence of this in the ICM (e.g., A. C. Fabian et al. 2000; R. E. A. Canning et al. 2010; M. McDonald et al. 2011). This multiphase gas could form in situ through a self-regulated feedback loop in which the central black hole heats the surrounding medium, while producing a wealth of thermal instabilities that cause some gas to cool, condense, and rain back down on the central black hole, reigniting the feedback loop (e.g., see the precipitation discussed in G. M. Voit et al. 2015, cold feedback in F. Pizzolato & N. Soker 2005, and *chaotic cold accretion* in M. Gaspari et al. 2013). The multiphase gas could also originate from cold gas that has been uplifted by the radio jets of the central black hole (e.g., B. R. McNamara et al. 2014) or as a result of both processes, as the low-entropy gas that has been uplifted by the radio jet becomes thermally unstable when it is lifted to higher altitudes (see the stimulated feedback model in B. R. McNamara et al. 2016).

In this work, we target the most extensively studied cluster of galaxies with multiphase gas in the literature, the Perseus cluster, located at a redshift of $z = 0.017284$ (A. C. Fabian et al. 2000; C. J. Conselice et al. 2001; A. C. Fabian & J. S. Sanders 2006; N. A. Hatch et al. 2006; P. Salomé et al. 2008; R. E. A. Canning et al. 2010; Hitomi Collaboration et al. 2016). Due to its proximity and extensive multiwavelength coverage, we studied the optically emitting cool gas in this target with exquisite spatial resolution ($116 \text{ pc pixel}^{-1}$).

Perseus also exhibits powerful radio jets that are cospatial with cavities as seen at X-ray wavelengths in the ICM (e.g., R. F. Mushotzky et al. 1981; A. C. Fabian et al. 2002; R. W. Schmidt et al. 2002; E. Churazov et al. 2003; J. S. Sanders et al. 2004). Several studies indicate that the cooling of the ICM, which would result in a cooling flow, is being halted by the injection of energy. This energy is introduced by jets emanating from the active galactic nucleus (AGN) of the central galaxy from the large scales to the small scales through a process of turbulent cascade of energy. Consequently, making the cluster a prototype for radio mode feedback (e.g., A. C. Fabian & J. S. Sanders 2006). Moreover, these types of clusters with AGN feedback have been found to host filamentary nebula of cool gas (e.g., M. McDonald et al. 2011).

Indeed, the central dominant galaxy, NGC 1275 is surrounded by a spectacular nebula of multiphase gas, first reported in R. Minkowski (1959). This work, and subsequent imaging, revealed the size of the nebula, which covers an area of $80 \text{ kpc} \times 50 \text{ kpc}$ corresponding to $218'' \times 136''$. Follow-up observations reveal the presence of an interloping galaxy, referred to as the high-velocity system (HVS), seen in projection and that is believed to be infalling on NGC 1275. In velocity space, the HVS is offset by an impressive 3000 km s^{-1} with respect to the central galaxy NGC 1275

(e.g., R. Minkowski 1959; R. Lynds 1970; V. C. Rubin et al. 1977; C. J. Conselice et al. 2001; A. P.-Y. Yu et al. 2015).

The multiphase nebula in Perseus is associated with warm ionized gas (10^4 K), seen through optical emission lines such as $H\alpha$ and $[\text{N II}]\lambda 6583$. Hubble Space Telescope (HST) observations have additionally revealed that certain filamentary structures (such as the large and small northern filament; see Figure 1) are extremely thin, on the order of 70 pc in diameter, while extending 6 kpc in length (A. C. Fabian et al. 2008). Importantly, these results suggest the presence of strong magnetic fields that stabilize the ionized gas filaments. Follow-up UV observations taken with the HST confirmed an overall lack of young stars indicating that the origin of the nebula is not dominated by star formation, except for small knots in the northern filament and in the region called the blue loop (R. E. A. Canning et al. 2010). In light of the HVS, this filamentary nebula of gas at the same redshift of NGC 1275 is often referred to as the low-velocity system (LVS).

In E. M. Burbidge & G. R. Burbidge (1962), the authors observed that the $[\text{N II}]$ to $H\alpha$ ratio was near unity in NGC 1275 and argued that photoionization by O and B stars was insufficient to explain this higher-than-usual ratio. Subsequent works have found similar results (e.g., N. A. Hatch et al. 2006; M. Gendron-Marsolais et al. 2018; B. Vigneron et al. 2024). Rather, a ratio of unity between these lines is more prominent in the nuclei of galaxies (e.g., R. L. Davies et al. 2014; C. M. Dickey et al. 2019; K. Oh et al. 2019). Interestingly, consistent values around unity of the $[\text{N II}]/H\alpha$ ratio are found well away from the AGN of NGC 1275.

The role of the AGN in ionizing the extended, optically emitting cool filaments surrounding NGC 1275 has been a subject of debate. Decades of observations have demonstrated the relatively limited influence of its activity as an ionizing source, rather suggesting a possible role in affecting only the inner few kiloparsecs of the filamentary structure. The first dedicated spectroscopic studies of NGC 1275's filaments originally proposed that shocks and the central AGN radiation could potentially ionize the optical filaments (S. M. Kent & W. L. W. Sargent 1979). However, subsequent spectroscopic observations led to the exploration of multiple other potential ionization mechanisms. Additionally, these analyses further concluded that NGC 1275's AGN would be unable to ionize the optical filamentary nebula and that a combination of other ionization sources could explain the filaments' emission profiles (see T. M. Heckman et al. 1989, B. M. Sabra et al. 2000 and C. J. Conselice et al. 2001). Nevertheless, more recent spectroscopic studies of the cool filaments surrounding NGC 1275 tentatively suggested that the central regions close to the brightest cluster galaxy (BCG) could be partly affected by the AGN's activity, or a similarly hard excitation source (see N. A. Hatch et al. 2006 and M. Gendron-Marsolais et al. 2018).

The kinematics of the multiphase nebula were first measured by C. J. Conselice et al. (2001) using the DensePak fiber array at the WIYN observatory.¹⁷ These measurements revealed a complex velocity structure of the warm $H\alpha$ -emitting gas in the center of NGC 1275. Carefully selected slit spectroscopy along the filamentary structure in NGC 1275 by the Gemini Multi-Object Spectrometer further demonstrated the complexity of the kinematics of the system (N. A. Hatch et al. 2006). The first complete view of the kinematics of NGC 1275 was published

¹⁷ The WIYN observatory hosts a 3.5 m telescope and is located at the Kitt Peak National Observatory in Southern Arizona.

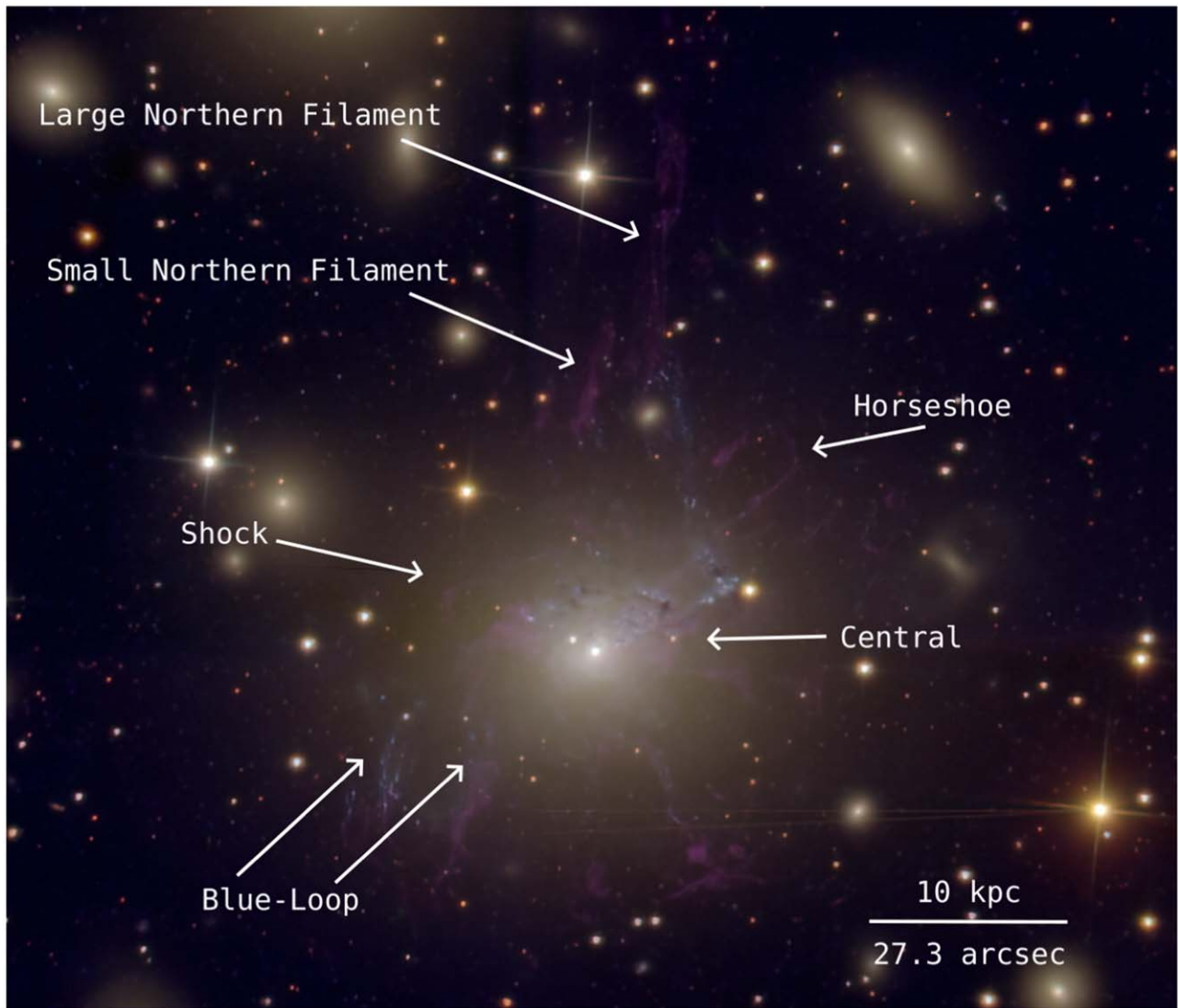


Figure 1. Composite image of the SN 1 (365–385 nm; blue), SN 2 (480–520 nm; green), and SN 3 (651–685; red) filters emission in NGC 1275 obtained with SITELLE on the CFHT. We constrain the image only to cover approximately a quarter of the SITELLE field of view in order to highlight the optical emission nebula.

by M. Gendron-Marsolais et al. (2018); these observations were taken by the SITELLE instrument located at the Canada-France-Hawaii Telescope (CFHT). They revealed no organized rotation in the nebula. Follow-up high spectral resolution observations with SITELLE presented in B. Vigneron et al. (2024) revealed the presence of a disk-like central structure characterized by a high-velocity dispersion ($\geq 80 \text{ km s}^{-1}$). This structure also appears spatially correlated and comoving with a similar central disk of cold molecular gas as observed by J. Lim et al. (2008) with the Submillimeter Array. In contrast, the rest of the filamentary nebula displays a relatively low and homogeneous velocity dispersion ($20\text{--}40 \text{ km s}^{-1}$), potentially suggesting that multiple mechanisms might be at work to produce the multiphase gas within this galaxy cluster.

Observations taken with the Chandra X-ray Observatory also highlight the presence of the same filamentary structures in the soft band covering $0.5\text{--}2.0 \text{ keV}$ (e.g., A. C. Fabian et al. 2000; A. C. Fabian et al. 2003; A. C. Fabian & J. S. Sanders 2006). This cospatiality between the warm $\text{H}\alpha$ emitting gas and the hot X-ray emitting ICM has been confirmed through several papers exploring the multiphase gas (e.g., A. C. Fabian et al. 2003;

J. Lim et al. 2008; M. McDonald et al. 2011; Y. Li et al. 2020). It has also been extended to $\text{CO}(2\text{--}1)$ emission tracing the $20\text{--}500 \text{ K}$ molecular gas (P. Salomé et al. 2008; H. Nagai 2019) and far-infrared red atomic gas transitions such as $[\text{N II}]\lambda 122 \mu\text{m}$ tracing cold gas between 40 and 120 K (R. Mittal et al. 2012).

In this work, we present new additional SITELLE flux maps, targeting the $[\text{O III}]\lambda 5007$, $\text{H}\beta$, and $[\text{O II}]\lambda 3726 + [\text{O II}]\lambda 3729$ emission lines. These observations cover for the first time the entire filamentary nebula in NGC 1275 at these wavelengths. We use these maps to investigate the ionization mechanism of the nebula using standard and modified Baldwin–Phillips–Terlevich (BPT) diagrams (e.g., J. A. Baldwin et al. 1981). As discussed throughout the paper, it is difficult to fully constrain the ionization mechanism for the filaments using the BPT diagram. In Section 2, we present the observations and the data analysis methods. In Section 3, we present the flux maps for the SN 1, SN 2, and SN 3 filter observations in addition to the BPT diagrams. In Section 4, we explore individual regions of the nebula in detail and compare them with multiwavelength studies. Finally, we will summarize our results in Section 5 and discuss future work.

Table 1
The Filters and Their Properties Used in This Study

Filter	Wavelength (Å)	Emission Lines	Resolution: $R = \frac{\Delta\lambda}{\lambda}$	Observation ID	PI
SN 1	3650–3850	[O II]λ3276, [O II]λ3279	1800	17BC22	Gendron-Marsolais
SN 2	4800–5200	Hβ, [O III]λ4959, [O III]λ5007	1800	17BC22	Gendron-Marsolais
SN 3	6510–6850	Hα, [N II]λ6548, [N II]λ6583, [S II]λ6716, [S II]λ6731, [O I]λ6364	1800	16BQ12	Morrison

Note. Description of SITELLE filters used in this study including the observation IDs and Principal Investigator (PI) indicated on the proposal. We note that the SN 3 data was part of the science verification stage.

We assume a redshift of $z = 0.017284$ for the LVS of NGC 1275, corresponding to $21.1 \text{ kpc arcmin}^{-1}$ (E. L. Wright 2006; Hitomi Collaboration et al. 2018). Assuming the Hubble constant of $H_0 = 69.6$, the energy density of matter, $\Omega_M = 0.286$, the energy density of the vacuum, $\Omega_{\text{vac}} = 0.714$, and a flat curvature, this redshift is equivalent to a luminosity distance of 75.5 Mpc.

2. Observations and Data Reduction

2.1. SITELLE at the CFHT

NGC 1275 was observed in 2017 with the SN 1 (3650–3850 Å) and SN 2 (4800–5200 Å) filters with a spectral resolution of $R \approx 1800$ (PI: Gendron-Marsolais). The SN 1 filter targets the [O II]λ3726,3729 emission-line doublet, while the SN 2 filter captures [O III]λ4959, [O III]λ5007, and Hβλ4861. As for the SN 3 (6510–6850 Å) filter, NGC 1275 was initially observed as part of the science verification of SITELLE with a spectral resolution $R \approx 1800$ (PI: Morrison). Although NGC 1275 has since been reobserved at a higher resolution ($R \approx 7000$; PI: Rhea & Hlavacek-Larrondo; B. Vigneron et al. 2024), we use here the initial data since it has the same spectral resolution as the other two cubes. The SN 3 filter targets several prominent emission lines: Hαλ6563, [N II]λ6548, [N II]λ6583, [S II]λ6716, [S II]λ6731, and [O I]λ6364. A summary of the filters, emission lines targeted, resolution, observation ID, and PIs can be found in Table 1. We show a composite image in Figure 1 highlighting the regions of interest. Each pixel of SITELLE corresponds to a projected size of approximately $113 \text{ pc} \times 113 \text{ pc}$ ($0''.32 \times 0''.32$) on the sky at the redshift of NGC 1275.

The data for all three filters were reduced and calibrated using the ORBS data pipeline (T. Martin & L. Drissen 2017). The data analysis presented in this paper was completed using LUCI (C. Rhea et al. 2021b; C. L. Rhea et al. 2021c). LUCI is a general-purpose line-fitting algorithm conceived specifically for SITELLE. LUCI uses machine learning algorithms trained to predict the velocity and velocity dispersion of emission lines present in a SITELLE spectrum to initialize an optimization algorithm that fits a model to the observed spectrum. Following T. B. Martin et al. (2016), we fit a sinc function convolved with a Gaussian function to each emission line. The sinc-Gauss function is written as follows:

$$\text{SG}(x) = Ae^{-b^2} \frac{\text{erf}(a - ib) + \text{erf}(a + ib)}{2\text{erf}(a)}, \quad (1)$$

where

$$a = \frac{\Delta\sigma}{\sqrt{2}\Delta w} \quad (2)$$

and

$$b = \frac{x - x_0}{\sqrt{2}\Delta\sigma}, \quad (3)$$

where x is the position, x_0 is the rest position of the line, A is the maximum value, Δw is the width of the sinc function, and $\Delta\sigma$ is the width of the Gaussian function.

Since we provide the redshift of the filamentary nebula to LUCI, the fitting process excludes the HVS.

The continuum is fitted assuming a zeroth order polynomial. LUCI utilizes the `scipy.optimization.minimize` implementation of the sequential least squares programming algorithm. The machine learning algorithm in LUCI was trained on synthetic data covering a Doppler velocity of -500 – 500 km s^{-1} and a broadening ranging from 10 to 300 km s^{-1} . These bounds were chosen based on the kinematic maps previously obtained by M. Gendron-Marsolais et al. (2018). For more details on the machine learning algorithm and synthetic spectra, we direct the reader to C. Rhea et al. (2020) and Pamplemousse.¹⁸ Instead of obtaining point estimates from a convolutional neural network, we use the mixture density network described in C. Rhea et al. (2021a) to obtain error estimates on the line position and broadening. These are then passed into the fitting algorithm as priors to constrain the fits. This process is described in detail in C. Rhea et al. (2021a).

Each filter was fit separately with a spatial binning of 3×3 ($\approx 350 \text{ kpc} \times 350 \text{ kpc}$). The binning was chosen to maximize the detection of the emission lines, especially those present in SN 1 and SN 2, which are typically fainter than those present in SN 3. For the SN 3 and SN 2 filters, the velocity and velocity dispersion of the emission lines in the same filter were linked; in doing this, we explicitly assume that the same gas is responsible for these emission lines. In SN 1, each emission line’s velocity and velocity dispersion are tied together for the [O II] doublet, but due to the low spectral resolution, we are unable to disentangle the two components of the [O II] doublet (i.e., λ3726,3729), and thus, the flux reported is the summed flux of the two lines.

Before fitting the lines, we subtract the sky contribution from each filter. The sky spectra are taken from a $9''.6$ region centered at (3:19:42.4979, +41:32:01.810); this region contains neither point sources nor source emission. We show the sky spectra and fits in Figure 2. The LUCI fit commands used can be found in Appendix B. After fitting each data cube, we then apply an alignment and masking procedure on the fitted maps. Since the astrometry of each reduced SITELLE data cube is imperfect, we align the SN 1 and SN 2 observations to SN 3 using `astroalign.apply_transform` (M. Beroiz et al. 2020).

¹⁸ <https://sitelle-signals.github.io/Pamplemousse/index.html>

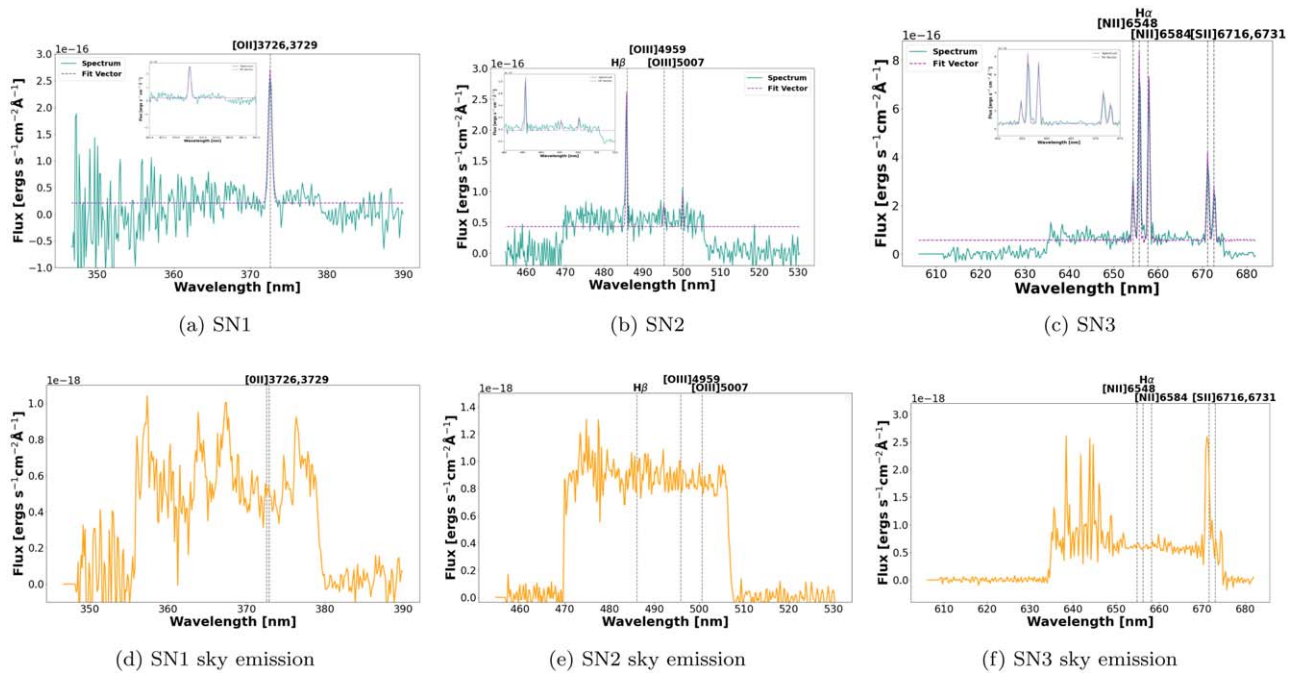


Figure 2. Illustrative SN 1 (a), SN 2 (b), and SN 3 (c) spectra (blue) and corresponding fit (purple). The spectrum is integrated from a square region containing 9 pixels (3×3 bin) centered at (3:19:49.7, +41:30:45.4) corresponding to the left-hand side of the central region. The bottom row shows the SN 1 (d), SN 2 (e), and SN 3 (f) sky emission spectra (orange). Here, the spectrum is integrated from a circular region centered at (3:19:42.4979, +41:32:01.810) with a radius of $9''.6$.

We supply three manually selected reference stars present in all three filters. Finally, we verify the alignment with Chandra observations. To align the observations, we use the position of the AGN and two other bright sources present in both the SITELLE deep images and the Chandra observation.

After the alignment, we apply a mask on each emission-line map to highlight the nebular emission in final maps. The mask consists of a flux cut of $1 \times 10^{-17} \text{ erg s}^{-1} \text{ cm}^{-2} \text{ \AA}^{-1}$ on all maps. Additionally, we apply a signal-to-noise ratio (SNR) cut of 3 (e.g., G. R. Tremblay et al. 2018; L. Rousseau-Nepton et al. 2019). We calculate the SNR after sky subtraction.¹⁹ The signal is calculated as the peak flux in the spectrum while the noise is sampled from a region of the spectrum not containing any emission lines. The SNR was calculated for each line except for the [N II] doublet. For the [N II] doublet, we assumed the same SNR as $H\alpha$ since the lines are crowded in the same region of the spectra. Finally, we apply an additional mask to the [O III] $\lambda 5007$ map since we needed to exclude the spaxels that overlap with the position of the HVS. Indeed, the [O III] $\lambda 5007$ emission from the nebula is unfortunately heavily contaminated by the [O III] $\lambda 4959$ emission from the HVS (N. A. Hatch et al. 2006) due to the velocity shift between the systems (The [O III] $\lambda 4959$ emission from the HVS is located at approximately 5097 \AA while the [O III] $\lambda 5007$ emission from the nebula is at 5094 \AA). This contamination is due to the spatial and spectral overlap of these lines. The position of the HVS was determined by fitting the $H\alpha$ in the HVS in the SN 2 filter. The resulting flux maps for the emission lines in each filter are shown in Figure 3.

2.2. Chandra X-Ray Observatory

The Chandra X-ray Observatory observations presented in this paper were taken with the Advanced CCD Imaging Spectrometer

(ACIS) using the FAINT mode. We use the following ObsIDs: 3209, 4289, 4946, 4947, 6139, 6145, 4948, 4949, 6146, 4950, 4951, 4953, 11713, 12025, 12036, 12037, 11714. The total combined exposure time is 1.16 Ms. Each observation was cleaned using a standard methodology implemented using the CIAO v4.14 software. The level-one event files were first processed using `lc_sigma_clip` to remove any background X-ray flare events. Then the data were reprocessed using the `chandra_repro` command with `vfaint=true` to take into consideration the diffusion nature of the emission. Background images were constructed using the `blanksky` routine. Finally, we created a background-subtracted, exposure-corrected, merged image using `merge_obs` on the soft band (0.5–2.0 keV). The details of the cleaning process can be found in C. L. Rhea (2020). Each pixel in the resulting combined image is approximately $176.5 \text{ pc} \times 176.5 \text{ pc}$, corresponding to a single instrument pixel ($0''.496 \times 0''.496$) of the Chandra ACIS detectors.

3. Results

3.1. Emission-line Fits

In Figure 2, we show the spectrum and the fit for a 3×3 binned spaxel in the central region that contains detectable emissions in SN 1, SN 2, and SN 3; additionally, we show the sky spectrum for each filter.

The fit of SN 1 (panel (a)) demonstrates that the [O II] doublet is in fact present and the two components are indistinguishable. Similarly, the SN 2 fit (panel (b)) shows the strong presence of $H\beta$, the weak presence of [O III] $\lambda 5007$, and the non-detection of [O III] $\lambda 4959$ as previously reported in N. A. Hatch et al. (2006). Panel (c) showing the SN 3 fit marks the presence of the strong $H\alpha$ and [N II] $\lambda 6583$ and relatively strong [S II] doublet.

¹⁹ We use the following command `LUCI.create_SNR_map(method=1)`.

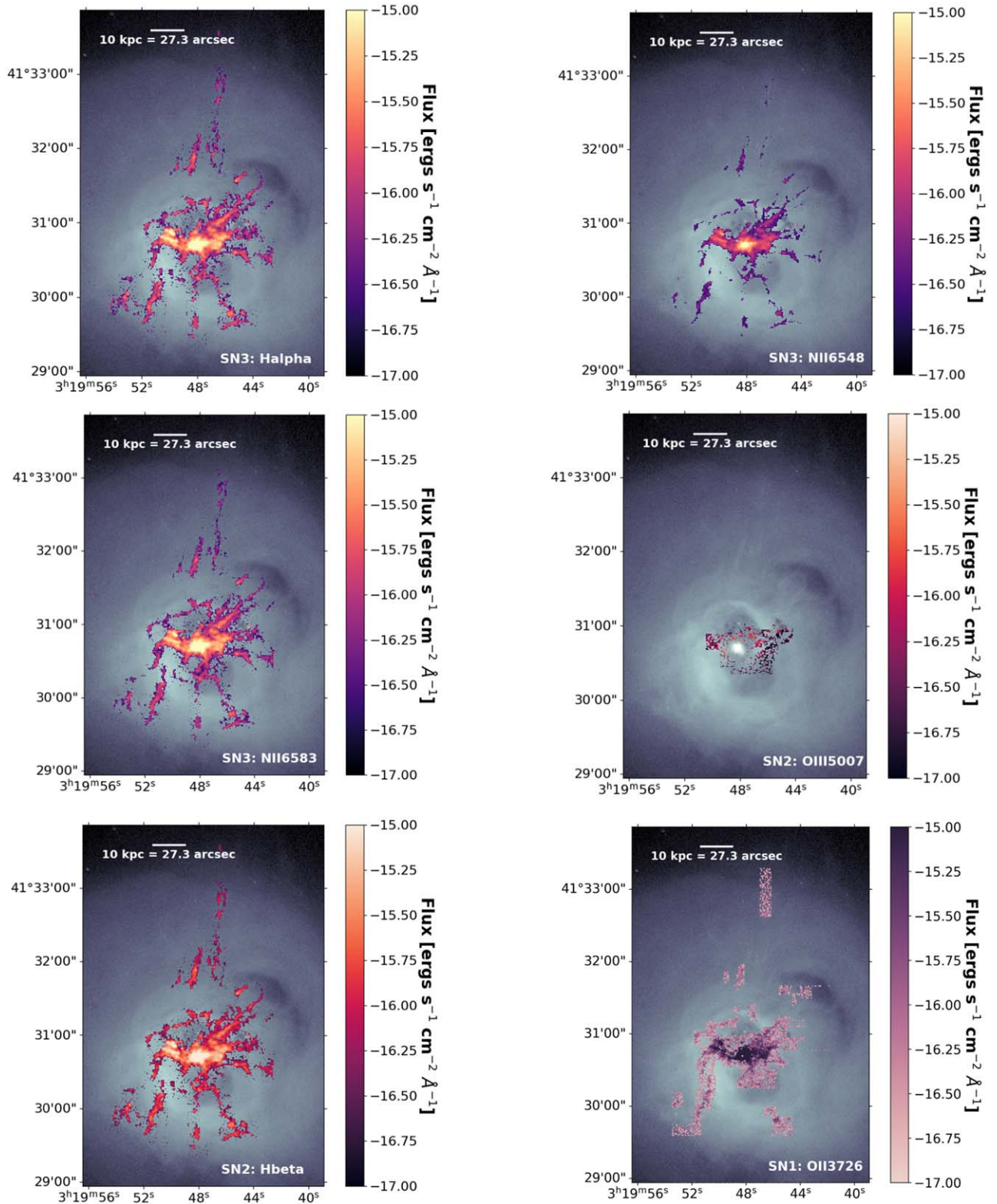


Figure 3. Masked flux maps for each emission line in SN 3, SN 2, and SN 1: $H\alpha$, $[N II]\lambda 6548$, $[N II]\lambda 6583$, $[O III]\lambda 5007$, $H\beta$, $[O II]\lambda 3726+[O II]\lambda 3729$. The calculated flux maps are masked below a SNR of 3 and a flux cut at $1 \times 10^{-17} \text{ erg s}^{-1} \text{ cm}^{-2} \text{ \AA}^{-1}$. Remaining noisy pixels were removed manually using `ds9`. In the background, we display the exposure-corrected, background-subtracted, merged Chandra image. The images are aligned to approximately 0.7.

Figure 3 shows the flux map for each emission line. Similar to the results presented in M. Gendron-Marsolais et al. (2018), both the $H\alpha$ and $[N II]\lambda 6583$ emission are omnipresent throughout the nebula in the form of extended filamentary

structures reaching dozens of kiloparsecs from the central region. In this work, we did not mask the AGN and can report the strong presence of the $H\alpha$ and the $[N II]\lambda 6583$ throughout the central regions.

With the SITELLE data, we can mostly separate the HVS from the emission of NGC 1275 because they have distinct velocities (e.g., C. J. Conselice et al. 2001). Despite this, a peculiar feature in the flux maps is the lack of nebular emission (from the LVS associated with NGC 1275) in regions overlapping with the HVS. We compared these regions with HST imaging (i.e., C. J. Conselice et al. 2001) and found that the regions lacking nebular emission were cospatial with the dust lanes of the HVS as seen through HST imaging. Hence, it appears that the dust in the HVS absorbs significantly the nebular emission originating from NGC 1275, essentially obscuring it from SITELLE.

$H\beta$ is weakly detected in the nebula and is primarily concentrated in the central region surrounding NGC 1275. In Figure 3, we use the $H\alpha$ map to apply a filter on the $H\beta$ map; we do this only after verifying that the $H\beta$ emission follows the same contours. This process is done to reduce the amount of noise in the image. Moreover, $[O\text{ III}]\lambda 5007$ is predominant in the central regions but missing in the extended filaments. We discuss this further in Section 4.

Since the SN 1 observation does not have sufficient spectral resolution to disentangle the two components of the $[O\text{ II}]$ doublet, we combine their calculated fluxes (see Figure 3(f)). The flux map reveals the omnipresence of this strong emission line throughout the nebula. However, due to large errors in the flux owing to the low signal to noise, we are unable to draw conclusive results from trends in the $[O\text{ II}]$ emission.

3.2. Emission-line Classification

Emission-line ratios and equivalent widths have been used to classify emission-line nebulae. However, emission-line classification systems (BPT and WHAN) based on star-forming galaxies with and without AGN may fall short of a diagnostic for emission-line regions with more physical processes in play. We show that traditional classification systems may be useful in identifying properties that are similar to those observed in emission-line galaxies forming stars, but have limited diagnostic usefulness beyond that. We use traditional BPT diagram diagrams to plot emission-line ratios from the central portion of the nebula where $[O\text{ III}]$ is detected, and we find that the emission-line ratios in the central region are inconsistent with AGN photoionization or star formation as a sole source of energy and ionization. We show a weak trend of $[O\text{ III}]/H\alpha$ with distance from the AGN, which indicates that AGN photoionization may contribute to the ionization state of the gas very close to the AGN. But the constant $[N\text{ II}]/H\alpha$ ratio through the same region suggests that the dominant source of energy is more distributed. We use the WHAN diagram to inspect and classify $[N\text{ II}]/H\alpha$ emission-line ratios and $H\alpha$ equivalent widths. Inspection of the WHAN diagrams for the line emission from the even more extended nebular gas shows emission with high equivalent width (HEW) and $[N\text{ II}]/H\alpha$ ratios not that dissimilar from what is observed in the center. The range is broader, with a hint of an inverse relationship between equivalent width of $H\alpha$ and the $[N\text{ II}]/H\alpha$ ratio. We discuss these results in turn below.

3.2.1. Standard BPT Diagram

BPT diagrams are frequently used to study the ionization mechanism at play in emission-line nebula (e.g., J. A. Baldwin et al. 1981). The two standard BPT diagrams plot either $[N\text{ II}]$

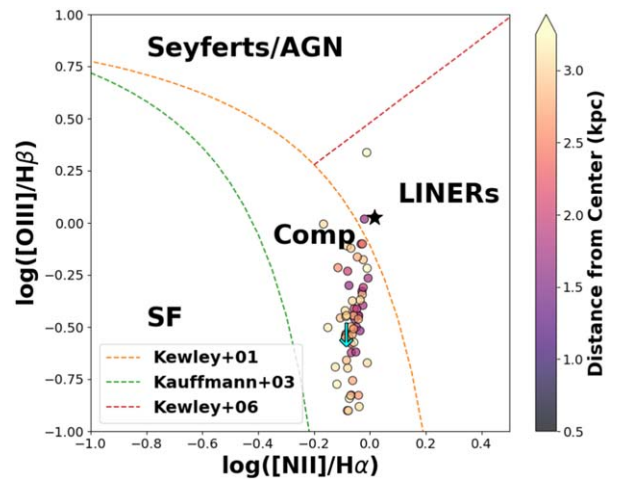


Figure 4. BPT diagram showing $\log([N\text{ II}]\lambda 6583/H\alpha)$ vs. $\log([O\text{ III}]\lambda 5007/H\beta)$ in the central region of NGC 1275. The points are color coded by their distance to the AGN at the center of NGC 1275. The cyan arrow represents the upper bound of the brightest pixel in the small northern filament. The AGN is marked by a black star. We overplot the L. Kewley et al. (2001, hereafter K01; purple), K03 (orange), and K06 (blue) diagnostic lines. The region between the K01 and the K03 lines is considered a composite region. Spaxels falling in the composite region are considered to be ionized by multiple types of ionizing sources with a range of characteristic average energy per ionization particle or photon.

$\lambda 6583/H\alpha$ or $([S\text{ II}]\lambda 6716 + [S\text{ II}]\lambda 6731)/H\alpha$ versus $[O\text{ III}]\lambda 5007/H\beta$. Since the edge of the filter and residual from the strong sky lines affect the quality of the fit of the $[S\text{ II}]$ doublet, we limit our analysis to the $[N\text{ II}]\lambda 6583/H\alpha$ versus $[O\text{ III}]\lambda 5007/H\beta$ BPT diagram.

While plotting emission-line ratios on precalibrated regions of BPT diagrams is traditionally done to attempt to differentiate star-forming regions from regions dominated by AGN, e.g., Seyferts and LINERS (G. Kauffmann et al. 2003, hereafter K03; L. J. Kewley et al. 2006, hereafter K06; G. Stasińska et al. 2006, hereafter S06), the literal classifications are only useful for emission-line nebulae where there are only two options for energy sources: AGN and stars. Figure 4 shows that even in the central portion of NGC 1275, all of the points lie in the “composite” region that suggests that even in the context of only two energetic candidates, some combination is needed. Therefore, we adopt a more data- and physics-centered approach.

However, these lines do not represent steadfast delineations between different types of ionization process. Instead, we adopt a more modern interpretation of the diagnostic lines that states regions in the star-forming area of the diagram must not have a highly energetic ionizing source while regions in either the strong AGN or weak AGN regions must include a highly energetic ionizing source (e.g., G. Stasińska et al. 2006; T. Garn & P. N. Best 2010; R. Cid Fernandes et al. 2011; M. Curti et al. 2022). Emission-line ratios indicating high $[O\text{ III}]/H\alpha$ indicate a high photoionization parameter, or a high ratio of ionizing photons to ambient gas density. A high $[N\text{ II}]$ ratio, on the other hand, for gas with low to no $[O\text{ III}]$, is a measure of the energy per ionization. $[N\text{ II}]$ is a significant radiative coolant of ionized gas, and its emission strength is more sensitive to the temperature of the gas than it is to nitrogen abundance. Additionally, the regions in the Seyfert/AGN area have a stronger highly energetic ionizing source than the regions in the LINER area. Moreover, it is possible, and

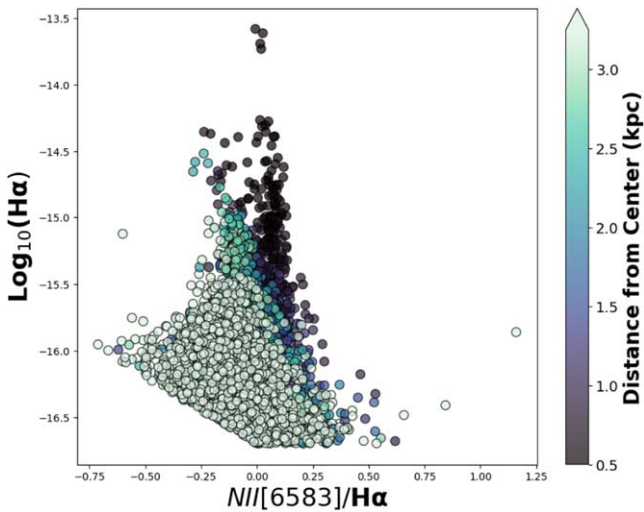


Figure 5. Emission-line diagram showing the relationship between $\log([\text{N II}]/\text{H}\alpha)$ and $\log(\text{H}\alpha)$ as a function of the distance from the AGN (designated here at the center) in kiloparsec. The central 0.5 kpc have been excised to remove any issues pertaining to multiple emission lines.

highly likely, that a combination of softer (i.e., photoionization) and highly energetic (i.e., cosmic rays or AGN activity) ionizing sources are required to ionize the bulk of the gas. Therefore, the position of the spaxel in the BPT diagram is simply indicative of the relative contribution of soft and highly energetic ionizing photons to the emission, if shocks and particle heating are not considered. It is important to note that high-energy photons have been demonstrated to reproduce emission-line ratios in the AGN region of the BPT diagram using CLOUDY simulations; we emphasize this point to indicate that a spaxel lying in the region traditionally denoted as AGN does not mean that an AGN is responsible for the ionization in this pixel (e.g., M. Donahue & G. M. Voit 1991).

Figure 4 shows the $[\text{N II}]\lambda 6583/\text{H}\alpha$ versus $[\text{O III}]\lambda 5007/\text{H}\beta$ BPT diagram. Since $[\text{O III}]\lambda 5007$ is only present in the central region of NGC 1275, the figure is only for the central region with the exception of the blue arrow. We measure the 3σ detection limit of $[\text{O III}]\lambda 5007$ for the brightest pixel in the small northern filament and include this point as a cyan arrow. The detection limit is calculated by taking a region of the spectrum not containing any lines and calculating the square root of the standard deviation of the flux in the region. Indeed, the trend highlighted in Figure 4 indicates that the $[\text{O III}]\lambda 5007$ emission falls off quickly as a function of the distance from the center. The points are color coded by their distance in kiloparsec to the AGN. The figure reveals two main takeaways: all points lie above the K03 line, and there is a clear trend in the position of the points in the diagram as a function of their distance from the AGN. First, it demonstrates that photoionization by AGN or by stars alone is not sufficient to explain the ionization of the gas. This is consistent with previous classifications of NGC 1275 as a Seyfert 1.5 type galaxy (e.g., D. E. Osterbrock 1981). Second, it indicates that the strength of the ionizing source decreases as a function of distance from the central AGN. We delve further into these in Section 4.1

In Figure 5, we show the relationship between $\log([\text{N II}]/\text{H}\alpha)$ and $\log(\text{H}\alpha)$ as a function of the distance from the AGN. The figure shows a distinct trend in the relationship as the spaxels become further from the influence of the central AGN. Spaxels

representing points nearest the AGN have consistent $[\text{N II}]/\text{H}\alpha$ ratios regardless of intrinsic $\text{H}\alpha$ brightness while points further from the AGN cover a wide range of ratios. This plot exposes a distinct population of points that are both bright and a considerable distance from the AGN (at least 2 kpc) with a characteristic $[\text{N II}]/\text{H}\alpha$ near 0. The population of distant filaments (more than 3 kpc from the center) with lower surface brightness do not have a single characteristic $[\text{N II}]/\text{H}\alpha$ ratio but rather have a notable spread in values.

3.2.2. WHAN Diagram

Since the $[\text{O III}]\lambda 5007$ emission in the extended nebula is too faint to be detected, we cannot rely on the standard BPT diagram to give a complete picture of the ionization mechanism in NGC 1275; therefore, we rely on the so-called WHAN diagram (e.g., R. Cid Fernandes et al. 2010; R. Cid Fernandes et al. 2011). The name WHAN comes from equivalent Width $\text{H}\alpha$ -Nitrogen). This diagnostic plot was constructed to investigate the main ionization mechanism in weak line galaxies (WLGs). WLGs are defined as galaxies for which a strong measurement ($\text{SNR} > 3$) of $[\text{O III}]\lambda 5007$ and/or $\text{H}\beta$ is impossible. Therefore, this plot serves as an appropriate choice for NGC 1275.

Although we refer the reader to R. Cid Fernandes et al. (2010) and R. Cid Fernandes et al. (2011) for a comprehensive dive into this diagram and how it compares with the standard BPT diagram, we recast the discussion on the discriminating lines in the WHAN diagram here since they are notoriously difficult to interpret. We again stress the need to not overinterpret these lines (e.g., G. Stasińska et al. 2006; T. Garn & P. N. Best 2010; R. Cid Fernandes et al. 2011; M. Curti et al. 2022). More precisely, the $[\text{N II}]/\text{H}\alpha$ diagnostic cuts do not delineate between stars and AGN but rather between pixels that are consistent with stellar photoionization and pixels where photoionization is unlikely to be the dominant source of energy.

Similar to standard the BPT diagrams, there are three separate diagnostic lines used to distinguish spaxels in which star formation (or the presence of massive O and/or B stars) can explain the measured line ratio as opposed to requiring a highly energetic ionizing source such as an AGN: K03, K06, and S06. Following the reasoning described in R. Cid Fernandes et al. (2011), we adopt the S06 line cut at $\log([\text{N II}]\lambda 6583/\text{H}\alpha) = -0.4$ such that any point to the left of this line falls in the star-forming category and any points to the right fall either in the Seyfert or LINER classification. Additionally, this line is not a hard cut-off, meaning not all spaxels to the left are star forming, and all to the right are not star forming (see G. Stasińska et al. 2006; R. Cid Fernandes et al. 2010; R. Cid Fernandes et al. 2011 for details). Rather, spaxels to the left of this line do not require a hard-ionizing source (HIS) to explain the line ratio. Similarly, we use the transposed K06 Seyfert/LINER diagnostic line which lies at $W_{\text{H}\alpha} = 6 \text{ \AA}$, where $W_{\text{H}\alpha}$ is the equivalent width and is defined as the $\text{H}\alpha$ flux over the continuum flux (e.g., N. Vale Asari et al. 2020). Any spaxel above this line is generally classified as an HEW and any spaxel below this line is classified as a low equivalent width (LEW). The distinction here comes from the fact that the equivalent width measures the ratio of the contributions of the highly energetic ionizer and the non-ionizing stellar component; therefore, the sHIS classification refers to a strong hard-ionizing agent, while a wHIS refers to a weaker hard-ionizing

agent. We do not use the standard nomenclature of strong AGN and weak AGN since, in the Perseus cluster, literature suggests that the AGN does not play a role in the ionization of the outer filaments (e.g., R. M. Johnstone & A. C. Fabian 1988). Rather, these regions are likely ionized by some other physical phenomena exhibiting a power-law spectrum such as from the cooling of hot X-ray gas or magnetic reconnection (e.g., G. J. Ferland et al. 2009; A. C. Fabian et al. 2011; N. Werner et al. 2014). We discuss the specifics of these mechanisms in Section 4.2.4. Instead, we use data-driven names such as HEW and LEW. Comparatively, the star-forming region does not require a hard-ionizing agent to explain the line ratio. There is an additional diagonal, dotted line below which measurements are uncertain (R. Cid Fernandes et al. 2011).

Figure 6 presents the WHAN diagram for NGC 1275. We show the position of each pixel in the WHAN plot color coded by the region to which they belong. Moreover, we overplot the mean value for each region and the associated 1σ error. The figure reveals that most points lie within the Seyfert designation. This implies that a relatively strong, highly energetic ionizing source is required to ionize the gas in these spaxels. On the right-hand side of the image, we present the spatial distribution of pixels color coded by their WHAN plot designation. We note that the vast majority of the nebula has a highly energetic ionizing agent (thus classified as Seyfert) while some boundaries of the inner filaments are characterized as LEW, implying that some boundaries seem to require a weaker hard-ionizing agent. We note, however, that the distinction of weak versus hard only stands for photon-based ionization and does not cover the scenario in which the ionizing source is from a different type of particle. Finally, the spaxels designated as star forming are primarily contained within the blue loop (R. E. A. Canning et al. 2010). We discuss each region of the nebula in more detail in Section 4.2.

4. Discussion

In this section, we discuss the results in the context of the standard BPT diagram, the WHAN diagrams, and overall trends.

4.1. Standard BPT Region Analysis

The middle right panel of Figure 3 shows that the $[\text{O III}]\lambda 5007$ flux in NGC 1275 is well constrained to the central regions of the galaxy, and we do not find it in the extended filaments. In Figure 4, we plot the $\log([\text{N II}]\lambda 6583/\text{H}\alpha)$ versus $\log([\text{O III}]\lambda 5007/\text{H}\beta)$ BPT diagram for the central regions of NGC 1275 color coded by the distance to the center of the galaxy. There is a clear trend that regions close to the center fall in the HEW and LEW regions and that the $\log([\text{O III}]/\text{H}\beta)$ ratio decreases as a function of the distance. Together, this indicates that while the ionizing source remains highly energetic, the strength of the source decreases further from the center. This strengthens the argument that the AGN at the center of NGC 1275 plays a role in the ionization of, at least, the central region of the nebula. Moreover, the BPT diagram reveals that photoionization from O or B stars is not sufficient to explain the ionized gas throughout the region where $[\text{O III}]$ is detected. In the filaments where we do not detect $[\text{O III}]$, the upper bound limit shows that the photoionization is again not sufficient to explain the ionization of the filaments. Moreover, when compared with the position of typical galactic regions on the standard BPT plot (see, for example, S. Veilleux & D. E. Osterbrock 1987), the position of

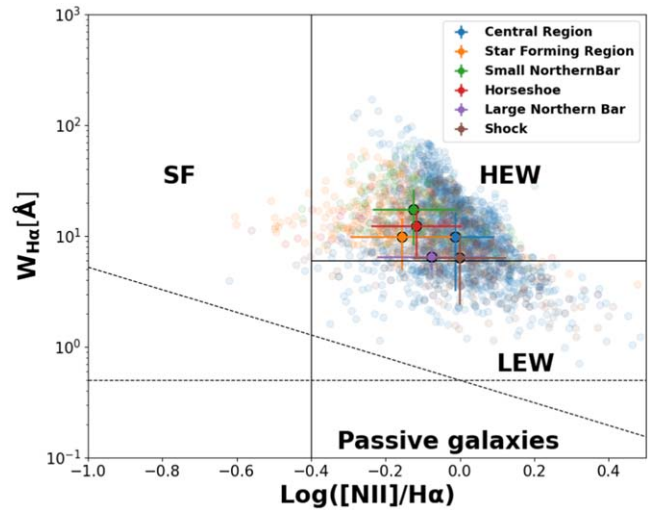


Figure 6. WHAN plot divided by structures. We show the ensemble of points color coded to each structure studied in detail in Section 4.2. For each structure, the mean value with a 1σ error is superimposed on the data points.

this upper bound indicates that the ionization mechanism at play in the outer filaments is distinct from ionized gas regions in our galaxy or nearby AGN.

4.2. WHAN Plot Analysis

Since the measurable $[\text{O III}]$ emission is constrained to the core of NGC 1275, we rely on the WHAN diagram described in Section 3.2.2 to analyze the ionization mechanism at larger scales in the nebula. We are also interested in the trends observed in the main structures previously identified in the nebula (see Figure 1).

In Figure 7, we show the WHAN diagram for all the spaxels in SN 3 that belong to the nebula and have an SNR greater than 3. On the right-hand side, we show the spaxels color coded by emission type as defined by their location in the WHAN diagram in R.A. versus decl.. Although the vast majority of the spaxels in the nebula lie within the Seyfert designation in the WHAN plot, there are populations of spaxels residing in the star-forming region and the LEW region. The majority of the star-forming spaxels fall within the blue loop as defined in R. E. A. Canning et al. (2010). The LEW spaxels are primarily located in the outskirts of the central region. Overall, this indicates that the equivalent width is not an accurate indicator of AGN activity since the outer filaments are not expected to be affected by the AGN.

In the left panel of Figure 8, we plot only spaxels categorized as HEW color coded by their $\log([\text{N II}]/\text{H}\alpha)$ value. The $\log([\text{N II}]/\text{H}\alpha)$ value is a proxy for the strength of the ionizing agent. On the right panel of Figure 8, we again plot the spaxels categorized as HEW but this time they are color coded by $W_{\text{H}\alpha}$.

Figure 6 shows the WHAN diagram of the nebula by the structures of interest. We have the following structures: the central region, the star-forming region, the small northern filament, the large northern filament, the horseshoe region, and the shock region (refer to Figure 1 for location of structures). In this figure, we have included the mean value and 1σ deviation for each structure. This reveals the regions of interest all lie well within the HEW categorization, implying a highly energetic and strong ionizing source for the majority of the spaxels in the structures. However, we note there are some

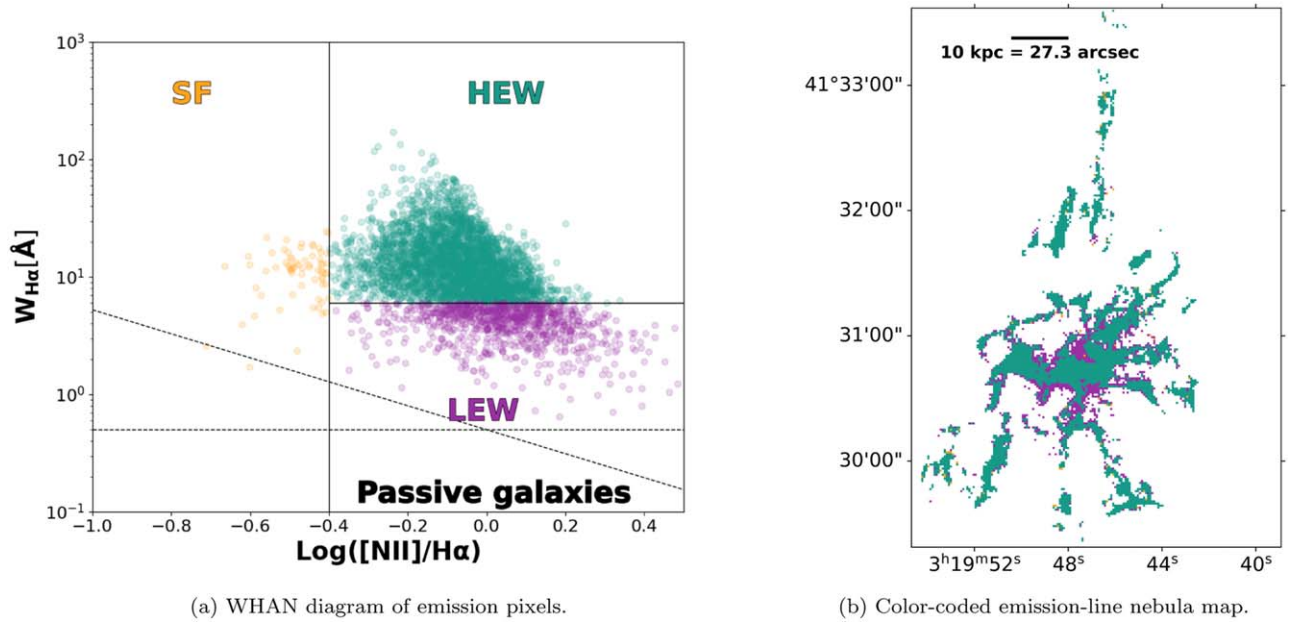


Figure 7. WHAN diagram and color-coded map for all pixels in the nebula surrounding NGC 1275 with an SNR over 3 and flux over $1e^{-17} \text{ erg s}^{-1} \text{ cm}^{-2} \text{ Å}^{-1}$. The pixels are divided into three categories: star forming (orange), HEW (teal), and LEW (purple). Measurements below the dotted line are considered uncertain (R. Cid Fernandes et al. 2011).

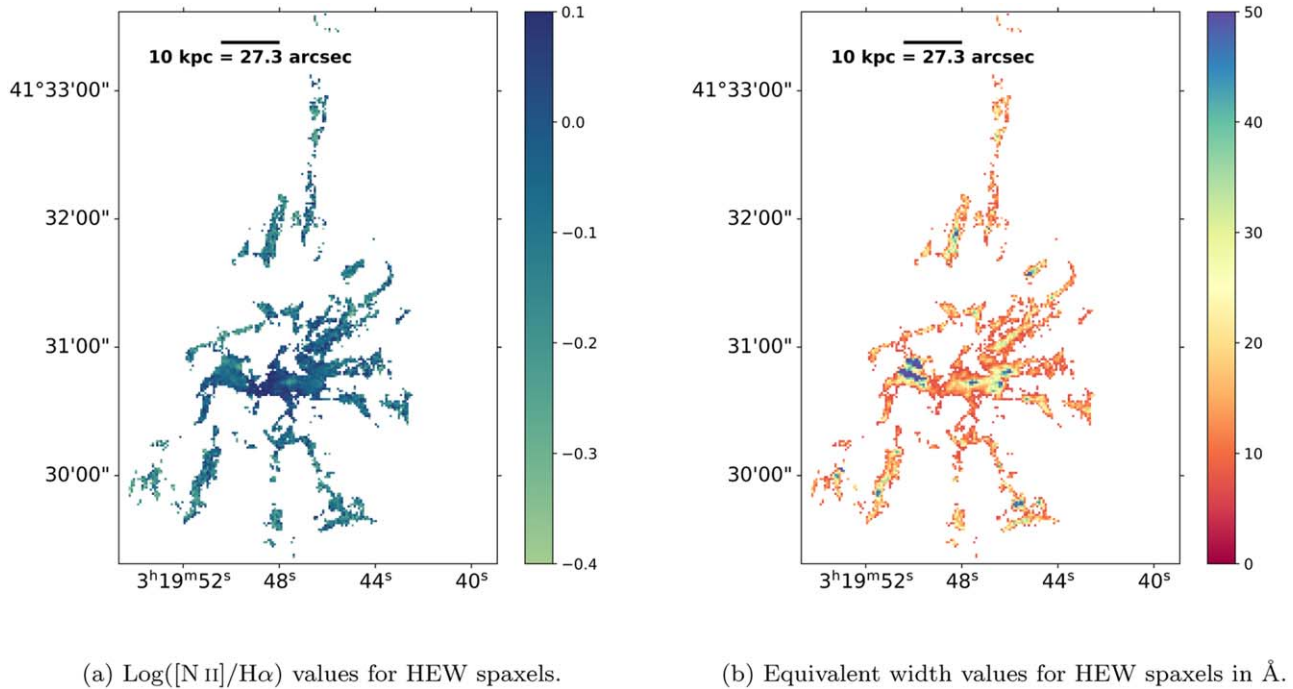


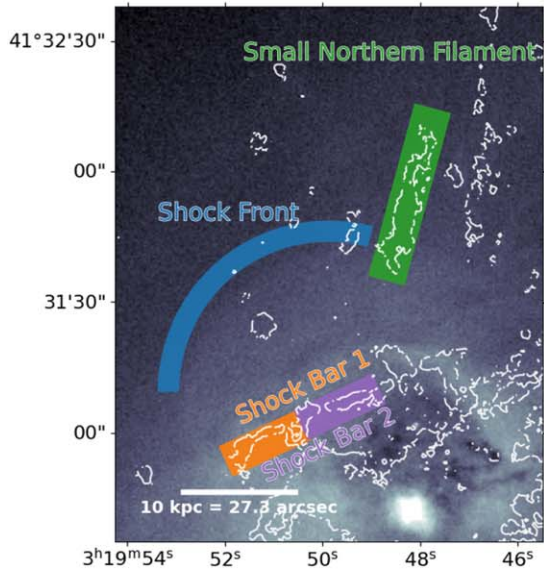
Figure 8. In the left-hand diagram, we plot the $\text{log}([\text{N II}]/\text{H}\alpha)$ values for spaxels labeled as HEW. Similarly, in the right-hand panel, we plot the equivalent width values for spaxels labeled as HEW in units of angstrom.

departures from the mean most notably in the shock region which contains more LEW spaxels and in the star-forming region where a handful of pixels fall within the star-forming sequence. The WHAN plots and morphology of these regions are studied individually in the subsequent subsections.

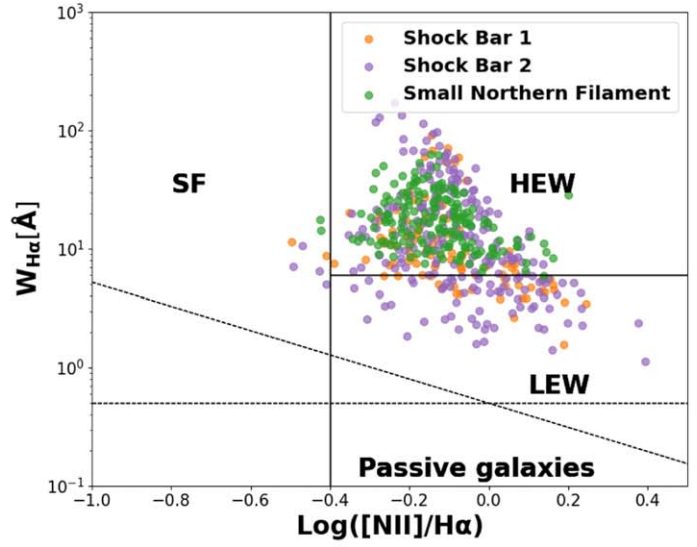
4.2.1. ICM Shock Structure

In Figure 9, we show a diagram of the shock structure using a soft X-ray image between 0.5 and 2.0 keV to highlight the extent of the ICM along with $\text{H}\alpha$ contours added in white. We

also added the location of the X-ray shock front as determined by A. C. Fabian & J. S. Sanders (2006) in blue, the small northern filament in green, and the structure of the nebula deemed the *shocked bar* in orange and purple. We divide the shocked bar into two distinct regions since the literature suggests there are two distinct filaments in this complex (N. A. Hatch et al. 2006). Our hypothesis is that the shocked bar has likely already been affected by the shock front while the small northern filament, with the exception of its most southern part, has not. Therefore, we expect to see the spaxels

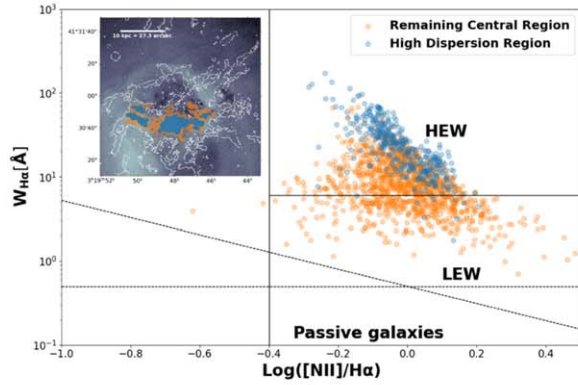


(a) Diagram of the shock region in NGC 1275.

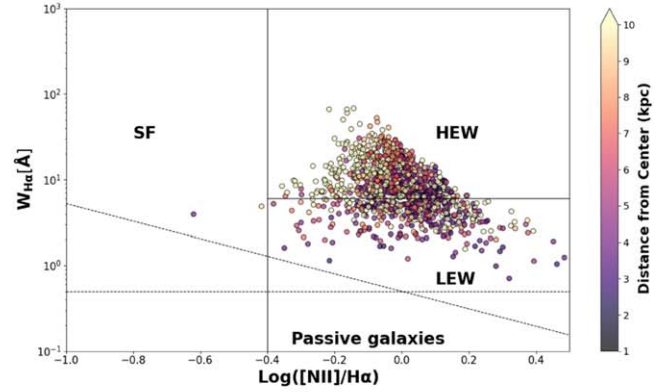


(b) WHAN plot for the bar in the shock region.

Figure 9. The left panel is a diagram of the shock region in NGC 1275. The background image is the Chandra soft X-ray emission between 0.5 and 2.0 keV described in Section 2.2; the contours highlight the $H\alpha$ emission. We highlight the location of the shock front (blue) as detected in A. C. Fabian & J. S. Sanders (2006). In the right-hand panel, we show the WHAN plot for the bar in the shock region (orange) and the small northern filament (green) that has not yet gone through the shock.



(a) Diagram of the central region of the filamentary nebula.



(b) WHAN plot color-coded by distance to the AGN.

Figure 10. The left panel is a diagram of the central region of the filamentary nebula in NGC 1275. The background image is the Chandra soft X-ray emission, while the white contours highlight the $H\alpha$ emission. We partition the central region into the high dispersion region as initially discovered in B. Vigneron et al. (2024) and the remaining pixels. We show the WHAN diagram for the high dispersion component (blue) and the remaining spaxels in the central region (orange). The right-hand panel shows the WHAN plot color coded by distance to the AGN.

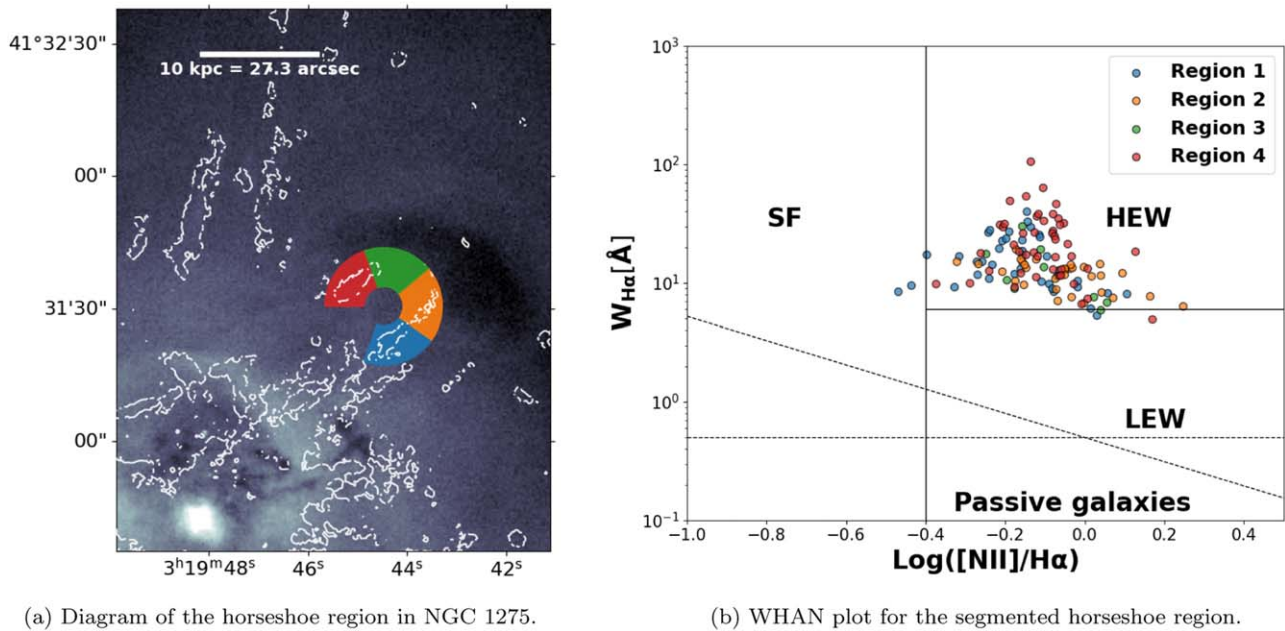
of each region occupying different spaces in the WHAN diagram. As evidenced on the right-hand side of Figure 9, these two regions both lie primarily within the HEW section of the diagram indicating that the ionization mechanism of these two regions is not distinct. There is, however, a slight difference since the shock bar contains spaxels well within the LEW section. In fact, a two-dimensional Kolmogorov–Smirnov test validates this hypothesis (J. A. Peacock 1983; G. Fasano & A. Franceschini 1987). This indicates that a portion of the shock bar does not require a strong, highly energetic ionizing source but rather a weaker, highly energetic ionizing source. Additionally, we tested if the ionizing source of the small northern filament changes as a function of distance from the base of the filament, yet we found no change. However, the large scatter in the shocked bar could indicate that the multiphase gas was affected by the passage of the shock.

Moreover, Figure 8 indicates that the $\log([NII]/Ha)$ value remains low and constant over the entire shocked bar.

4.2.2. Central Region

Figure 10 shows the WHAN plot for spaxels in the central region of NGC 1275. Furthermore, we divide the central regions into the high-velocity dispersion region,²⁰ initially identified in B. Vigneron et al. (2024), and the remaining spaxels in the center. B. Vigneron et al. (2024) found that this region is kinematically distinct from the rest of the nebula and is cospatial with the CO(2–1) disk of molecular gas reported in H. Nagai (2019). Spaxels are considered to be part of the high dispersion region if their flux is above

²⁰ We adopt the nomenclature of high dispersion region in order to be consistent with B. Vigneron et al. (2024).



(a) Diagram of the horseshoe region in NGC 1275.

(b) WHAN plot for the segmented horseshoe region.

Figure 11. Diagram and WHAN plot of the horseshoe region of the NGC 1275 filamentary nebula. The background image is the Chandra soft X-ray emission, while the white contours highlight the H α emission. The horseshoe is segmented into four color-coded sections, capturing the different morphological regions of the area. The colors on the diagram correspond to those in the WHAN plot.

$5 \times 10^{-16} \text{ erg s}^{-1} \text{ cm}^{-2} \text{ \AA}^{-1}$; this is similar to the distinction made in B. Vigneron et al. (2024). Although both groups of spaxels occupy the WHAN plot’s Seyfert area, the high dispersion pixels tend to have a higher equivalent width value, indicating a stronger ionizing source.

Furthermore, Figure 8 shows a structure in the $\log([\text{NII}]/\text{H}\alpha)$ values and $W_{\text{H}\alpha}$ that corresponds to the high dispersion region; in this region, the values are below unity while in the other parts of the central region are at or above unity. B. Vigneron et al. (2024) proposed that the high dispersion region originates from a distinct mechanism to the rest of the filaments, leading to more turbulent multiphase gas. Here, we see that this high dispersion region is consistent with a region requiring a highly energetic ionization source, perhaps from the AGN’s radio jets. Moreover, a two-dimensional Kolmogorov–Smirnov test reveals that these two populations are statistically distinct. In the last panel of the figure, we display each spaxel’s position in the WHAN diagram color coded by their distance from the AGN. There is a slight trend for softer sources the further away the spaxel is from the AGN, but this trend is tenuous.

Moreover, dedicated studies of the excitation mechanisms of cold molecular gas found in the inner regions of the filamentary structure surrounding NGC 1275 have been carried out. Indeed, multiple near-infrared spectroscopic observations at high resolution seem to indicate that the molecular gas found in the central 50 pc of the BCG appears to be excited either by shocks from the AGN activity or by X-ray heating from the central source (see R. J. Wilman et al. 2005; J. Scharwächter et al. 2013). Additionally, extended NIFS observations of the inner $900 \times 900 \text{ pc}^2$ reveal that powerful AGN-driven outflows could be at the source of the shocks necessary to ionize the inner molecular gas (R. A. Riffel et al. 2020). Interestingly, these results could reinforce the idea that the inner regions of the optical filaments close to the central BCG would require a highly ionizing source, most likely through AGN activity, as it can be observed for the central molecular gas.

4.2.3. Horseshoe Structure

Figure 11 highlights the emission around the horseshoe structure. The colored arcs highlight the horseshoe structure. These regions were chosen to analyze azimuthal trends in the ionization mechanism in different regions of the horseshoe. The results in the WHAN plot (right-hand panel) demonstrate that nearly all spaxels fall within the HEW region of the diagram, implying a source of ionization where the (energy/ionizing event) is higher than for ionizing photons from stars. The spaxels’ locations in the diagram are evenly distributed among the different regions. A. C. Fabian et al. (2003) posited that an X-ray bubble created the filamentary structure seen in the figure by dragging out previously ionized gas from the more central regions. While inconclusive, these results agree with that scenario since there is no spatial dependence within the horseshoe for the ionization mechanism.

4.2.4. Northern Filament

Figure 12 shows a map of the northern portion of NGC 1275 as seen through the lens of Chandra with white contours taken from the H α flux map; we highlight in yellow the location of the large northern filament. On the right-hand panel, we plot each spaxel in the large northern filament on the WHAN plot and color code them by the distance to the base of the filament. The majority of the points lie within the Seyfert region of the diagram. There are, however, a handful of spaxels lying in the star-forming region, which is consistent with results from R. E. A. Canning et al. (2010). Importantly, there is no trend in the ionizing mechanism as a function of distance from the base. This lack of a radial trend implies a distributed ionization mechanism is at play in the filament. Moreover, if the ionization came from the AGN, we would expect evidence for a highly energetic and stronger ionizing source nearer the base, which our data do not show. Therefore, we conclude that AGN photoionization is not responsible for powering the

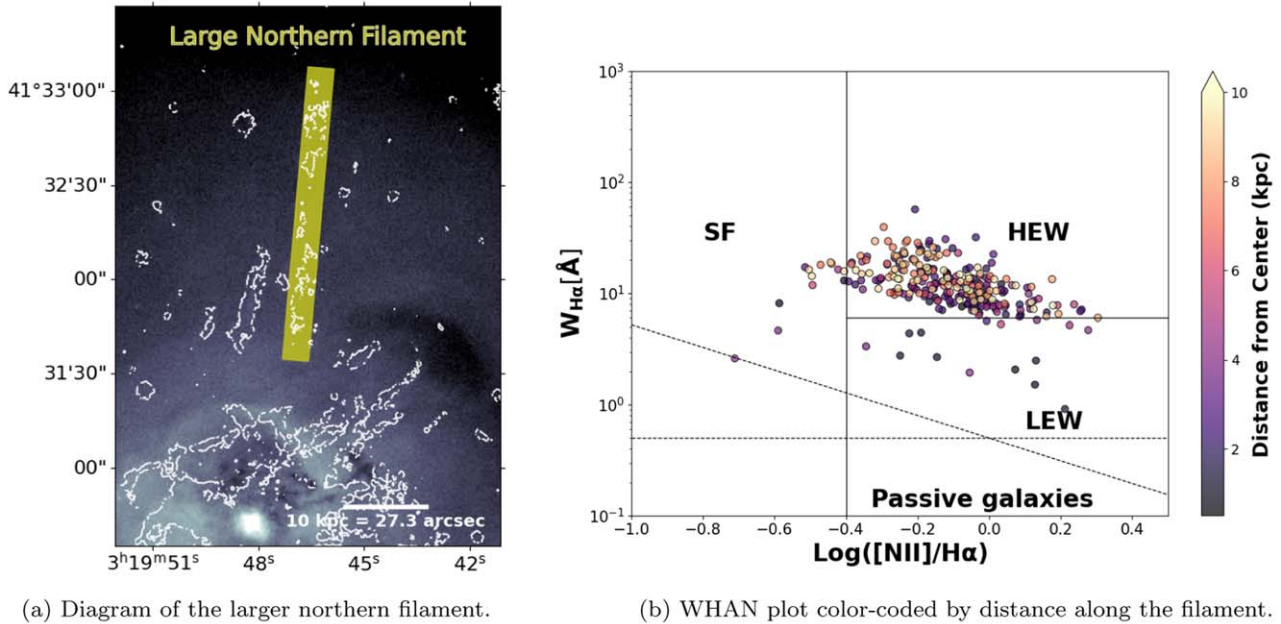


Figure 12. The left-hand plot is a diagram of the larger northern filament. The background image shows the soft X-ray emission captured by Chandra, with white contours following the H α emission. The WHAN plot on the right is color coded by the distance to the bottom of the filament.

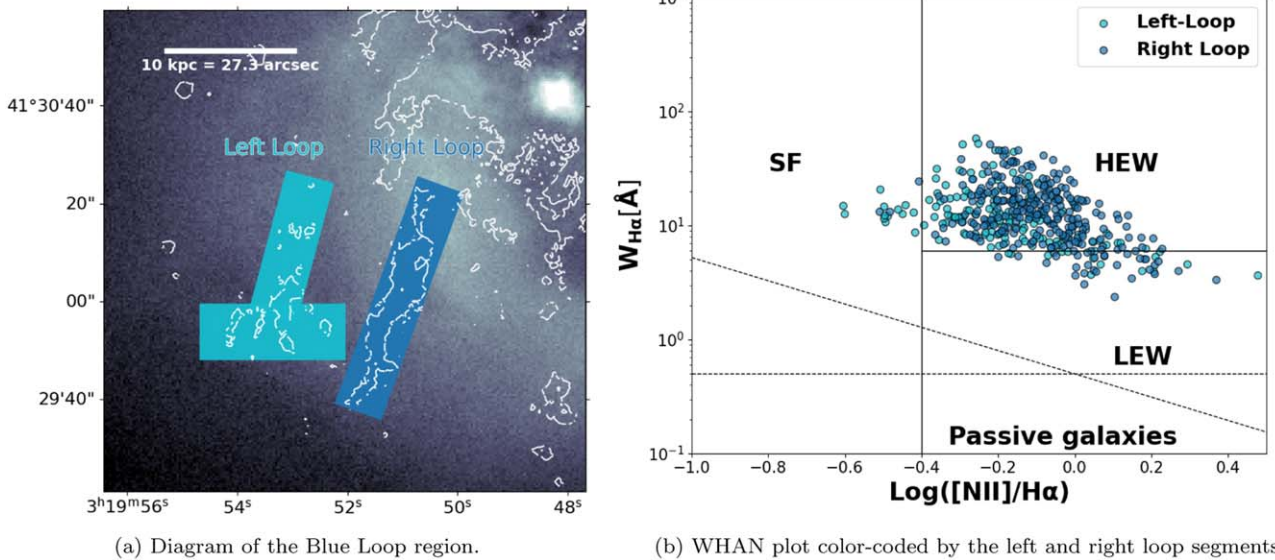


Figure 13. In the left panel, we have a diagram of the blue loop region. The background image shows the soft X-ray emission captured by Chandra, with white contours following the H α emission. The loop is segmented into a left and right loop. The WHAN plot is color coded by this distinction.

filaments. A uniformly distributed physical phenomenon that is an HIS appears to be responsible for the filaments.

Additionally, Figures 8 and 6 reveal a very small scatter in the equivalent width values in the northern filament compared to all other regions studied. This hints that the ionization mechanism is steady across the entire northern filament. The homogeneity in values across the northern filament, coupled with the fact that they are coincident with soft X-ray emission, supports the theory posited that the hot X-ray gas is responsible for the ionization of the cool filamentary gas (e.g., N. Werner et al. 2010; A. C. Fabian et al. 2011). Previous works have considered that the hot X-ray emitting particles ionize the cool gas; the particles penetrate the cool gas causing a cascade of secondary electrons that act as an ionizing agent for the cool

gas (G. J. Ferland et al. 2009; N. Werner et al. 2014). The hot ICM particles are potentially able to penetrate the cool gas initially through magnetic reconnection (e.g., A. C. Fabian et al. 2011). Simulations support the hypothesis demonstrating that collisional excitation and mixing are sufficient to explain the observation line ratios (e.g., R. E. A. Canning et al. 2016).

4.2.5. Star Formation in the Blue Loop

Figure 13 shows the blue loop as defined by R. E. A. Canning et al. (2010). We further subdivide the blue loop into a left loop and a right loop. The WHAN plot (right-hand panel) shows that the majority of the spaxels lie within the Seyfert region of the diagram, which indicates that a source highly energetic than photoionization is responsible for the ionized

gas. However, several spaxels lie within the star-forming region of the diagram, indicating that photoionization is sufficient to explain the ionized gas in these spaxels. This, along with the results from R. E. A. Canning et al. (2010), which show the presence of hot and young stars in the left loop, supports the presence of star-forming regions.

With regards to star formation throughout the nebula as a whole, there is little indication in the previous literature or from the findings presented here to indicate star formation occurring in traditionally observed regions such as H II regions in the disk of the galaxy. Instead, the regions where the data does hint at star formation are clumpy and in the outer filaments. Although previous studies on these type of optically emitting filamentary nebula surrounding BCGs have indicated that a mixture of shocks and star formation can account for the high $\log([\text{N II}]/\text{H}\alpha)$ values calculated here (e.g., M. McDonald et al. 2011), results from the literature indicate that star formation is not likely playing a crucial role in NGC 1275.

5. Summary

The central galaxy of the Perseus cluster, NGC 1275, plays host to an emission-line nebula visible clearly in optical wavelengths. The nebula is filamentary, ranging from the inner kiloparsecs to several dozens of kiloparsecs outward. While previous studies indicated a lack of star formation in most of the nebula (e.g., R. E. A. Canning et al. 2010), no robust and systematic study on the ionization mechanism of different regions across the entire nebula existed. In this paper, we use three SITELLE observations covering the majority of the optical regime to study the ionization mechanisms at play in the nebula. Though most regions of the nebula do not contain any [O III], a finding consistent with N. A. Hatch et al. (2006), we demonstrate that [O III] λ 5007 is present in the core of the emission-line nebula. Moreover, we find a slight radial trend in the strength of the ionizing source as a function of distance from the center of the cluster.

Due to the lack of detected [O III] emission in the extended filaments, we rely on the WHAN diagnostic plots (e.g., R. Cid Fernandes et al. 2010; R. Cid Fernandes et al. 2011), which do not require [O III] to distinguish between the ionization mechanisms. We find the following:

1. The large scatter in the shock bar implies that the shock has affected the ionization of multiphase gas.
2. The high dispersion region in the core requires a highly energetic ionizing source. This source may be from high-energy photoionization, shocks, or the cooling ICM.
3. The ionization in the horseshoe structure is homogeneous throughout.
4. The ionization mechanism in the northern filament is a strong and highly energetic ionizing source that is uniform across the filament.
5. There is little star formation occurring throughout the nebula.

6. The AGN does not play a critical role in the ionization of the filaments. While the exact extent of the AGN's role in the central regions of the nebula is not fully constrained, it is unlikely that it plays a crucial role beyond its immediate surroundings.

In this work, we have demonstrated the complexity of the ionization process throughout the different structures in the NGC 1275 filamentary nebula. Additionally, we have utilized this data set to map the optical emission of the entire nebula and bolstered the argument that some H II other than the central AGN is responsible for the ionization of the nebula. While illuminating, there remains much work to disentangle the different potential ionization processes.

Acknowledgments

The authors would like to thank the CFHT, which is operated by the National Research Council (NRC) of Canada, the Institut National des Sciences de l'Univers of the Centre National de la Recherche Scientifique (CNRS) of France, and the University of Hawaii. The observations at the CFHT were performed with care and respect from the summit of Maunakea, which is a significant cultural and historic site. C.L.R. acknowledges financial support from the physics department of the Université de Montréal, the MITACS scholarship program, and the IVADO doctoral excellence scholarship. J.H.-L. acknowledges support from NSERC via the Discovery grant program, as well as the Canada Research Chair program. M.L.G.M. acknowledges financial support from the grant CEX2021-001131-S funded by MCIU/AEI/10.13039/501100011033, from the coordination of the participation in SKA-SPAIN, funded by the Ministry of Science, Innovation and Universities (MCIU), as well as NSERC via the Discovery grant program and the Canada Research Chair program. M.M. acknowledges support from the Spanish Ministry of Science and Innovation through the project PID2021-124243NB-C22. This work was partially supported by the program Unidad de Excelencia María de Maeztu CEX2020-001058. M.N.W. is supported by the GACR grant 21-13491X. ACE acknowledges support from STFC (ST/T000244/1, ST/X001075/1).

Software: LUCI (C. L. Rhea et al. 2021c); ds9 (W. A. Joye & E. Mandel 2003); ndtest (Z. Li 2023); matplotlib (J. D. Hunter 2007); SciPy (P. Virtanen et al. 2020); NumPy (C. R. Harris et al. 2020); TensorFlow (M. Abadi et al. 2015); astropy (Astropy Collaboration et al. 2018; Astropy Collaboration et al. 2022); astroalign (M. Beroiz et al. 2020).

Appendix A Kinematics

In Figures 14–16, we show the kinematic fits (i.e., velocity and velocity dispersion) as calculated from SN 3, SN 2, and SN 1. The SN 2 maps follow the SN 3 maps closely. However, the SN 1 kinematic maps suffer from the fact that the O II doublet is not resolved. These results do not affect the flux in a meaningful way.

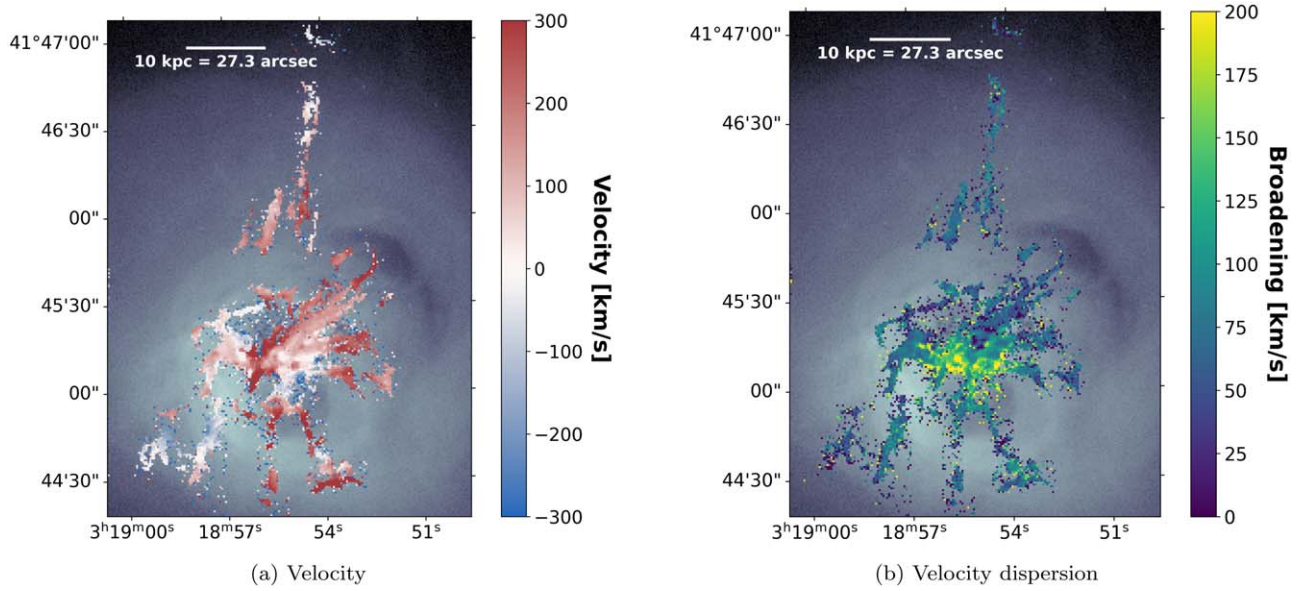


Figure 14. Left: SN 3 velocity map. Right: SN 3 broadening map. Although these findings were initially reported in M. Gendron-Marsolais et al. (2018), we include the LUCI-based fits here for posterity. We note that globally the values are similar to those calculated previously.

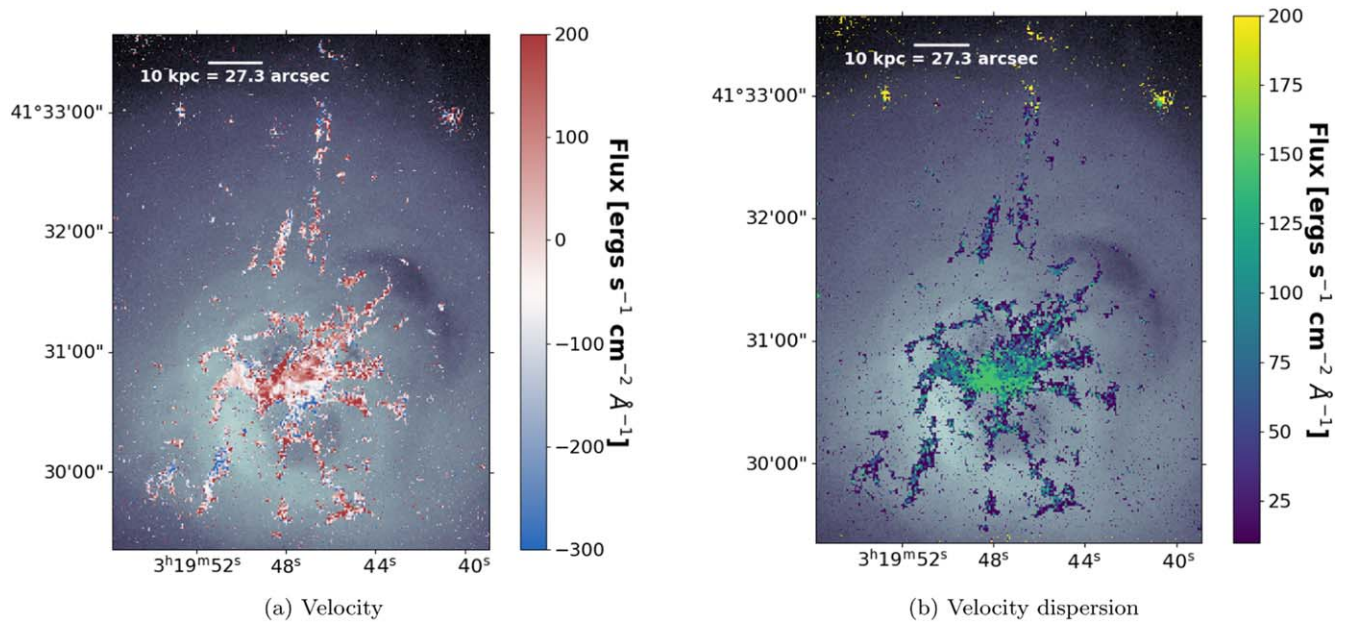


Figure 15. Left: SN 2 velocity map. Right: SN 2 broadening map. The values reported for the SN 2 data follow the SN 3 data closely.

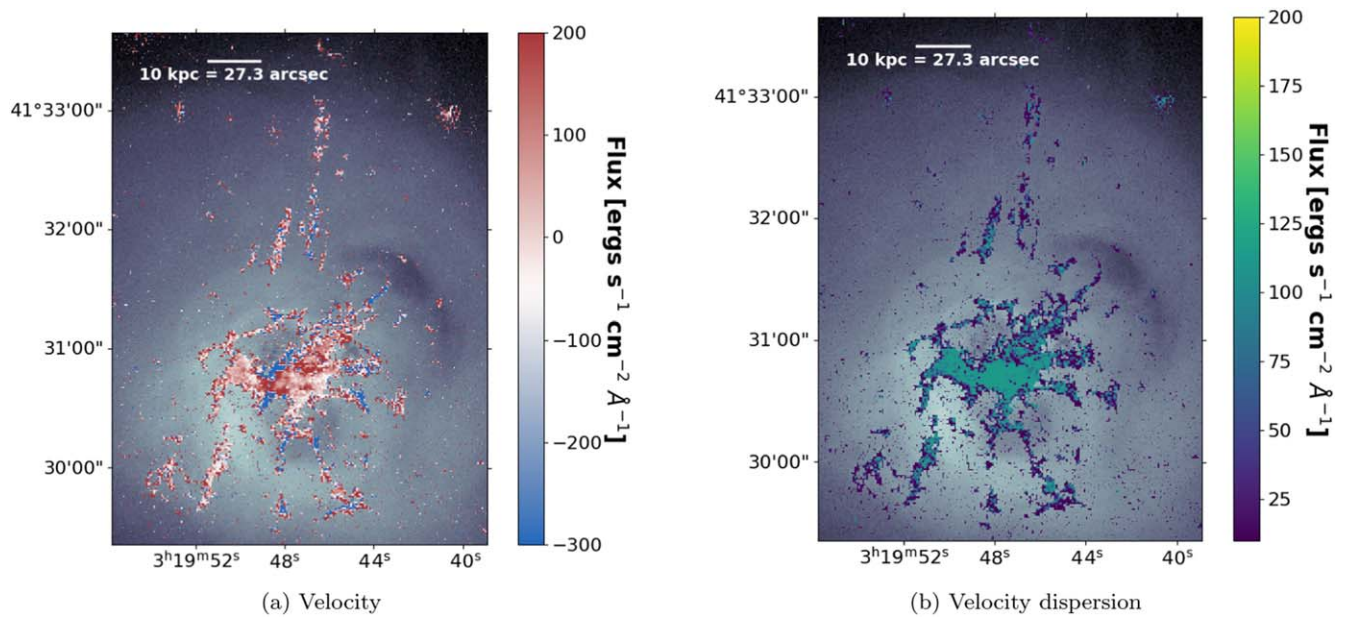


Figure 16. Left: SN 1 velocity map. Right: SN 1 broadening map. While the velocity values of the blended [O II] doublet follow the values reported for SN 2 and SN 3 closely, the broadening values differ. Instead, they are uniformly between 100 and 120 km s⁻¹. This is likely due to the fact that the two lines are completely blended.

Appendix B Fit Commands

In this appendix, we show the three LUCI commands used to fit each filter.

B.1. Command for Fitting SN 3

```

vel_map, broad_map, flux_map, chi2_fits = cube.fit_cube(
    ['Halpha', 'NII6548', 'NII6583', 'SII6716', 'SII6731'], # lines
    'sincgauss', # fit function
    [1,1,1,1,1], # velocity relationship
    [1,1,1,1,1], # sigma relationship
    1000, 1500, 200, 1000, # Bounds on pixels coordinates
    bkg=bkg_sky, # Apply background subtraction
    binning=3, # Binning
    n_threads=30, # Number of threads to run
    uncertainty=True,
    spec_min=15000, spec_max=15400
)

```

B.2. Command for Fitting SN 2

```

vel_map, broad_map, flux_map, chi2_fits = cube.fit_cube(
    ['Hbeta', 'OIII4959', 'OIII5007'],
    'sincgauss',
    [1,1,1],
    [1,1,1],
    800, 1300, 700, 1500,
    binning=3,
    bkg=bkg_sky,
    n_threads=12,
    uncertainty = True,
    spec_min=19750, spec_max=21500,
)

```

B.3. Command for Fitting SN 1

```

vel_map, broad_map, flux_map, chi2_fits = cube.fit_cube(
    ['OII3726', 'OII3729'],
    'sincgauss',
    [1,1], [1,1],
    800, 1300, 700, 1500,
    binning=3,
    bkg=bkg_sky,
    n_threads=12,
    uncertainty = True
)

```

ORCID iDs

Carter Lee Rhea  <https://orcid.org/0000-0003-2001-1076>
 Julie Hlavacek-Larrondo  <https://orcid.org/0000-0001-7271-7340>
 Marie-Lou Gendron-Marsolais  <https://orcid.org/0000-0002-7326-5793>
 Benjamin Vigneron  <https://orcid.org/0000-0002-2478-5119>
 Megan Donahue  <https://orcid.org/0000-0002-2808-0853>
 Auriane Thilloy  <https://orcid.org/0000-0001-5223-1888>
 Laurie Rousseau-Nepton  <https://orcid.org/0000-0002-5136-6673>
 Mar Mezcua  <https://orcid.org/0000-0003-4440-259X>
 Norbert Werner  <https://orcid.org/0000-0003-0392-0120>
 Jorge Barrera-Ballesteros  <https://orcid.org/0000-0003-2405-7258>
 Hyunseop Choi  <https://orcid.org/0000-0002-3173-1098>
 Alastair Edge  <https://orcid.org/0000-0002-3398-6916>
 Andrew Fabian  <https://orcid.org/0000-0002-9378-4072>
 G. Mark Voit  <https://orcid.org/0000-0002-3514-0383>

References

- Abadi, M., Barham, P., Chen, J., et al. 2015, 19
 Astropy Collaboration, Price-Whelan, A. M., Lim, P. L., et al. 2022, *ApJ*, 935, 167
 Astropy Collaboration, Price-Whelan, A. M., Sipőcz, B. M., et al. 2018, *AJ*, 156, 123
 Baldwin, J. A., Phillips, M. M., & Terlevich, R. 1981, *PASP*, 93, 5
 Barai, P., Viel, M., Borgani, S., et al. 2013, *MNRAS*, 430, 3213
 Beroiz, M., Cabral, J. B., & Sanchez, B. 2020, *A&C*, 32, 100384
 Bregman, J. N., Anderson, M. E., Miller, M. J., et al. 2018, *ApJ*, 862, 3
 Burbidge, E. M., & Burbidge, G. R. 1962, *ApJ*, 135, 694
 Canning, R. E. A., Fabian, A. C., Johnstone, R. M., et al. 2010, *MNRAS*, 405, 115
 Canning, R. E. A., Ferland, G. J., Fabian, A. C., et al. 2016, *MNRAS*, 455, 3042
 Churazov, E., Forman, W., Jones, C., & Böhringer, H. 2003, *ApJ*, 590, 225
 Cid Fernandes, R., Stasińska, G., Mateus, A., & Vale Asari, N. 2011, *MNRAS*, 413, 1687
 Cid Fernandes, R., Stasińska, G., Schlickmann, M. S., et al. 2010, *MNRAS*, 403, 1036
 Conselice, C. J., III, J. S. G., & Wyse, R. F. G. 2001, *AJ*, 122, 2281
 Curti, M., Hayden-Pawson, C., Maiolino, R., et al. 2022, *MNRAS*, 512, 4136

- Davies, R. L., Rich, J. A., Kewley, L. J., & Dopita, M. A. 2014, *MNRAS*, **439**, 3835
- Dickey, C. M., Geha, M., Wetzel, A., & El-Badry, K. 2019, *ApJ*, **884**, 180
- Donahue, M., & Voit, G. M. 1991, *ApJ*, **381**, 361
- Fabian, A. C., Celotti, A., Blundell, K. M., Kassim, N. E., & Perley, R. A. 2002, *MNRAS*, **331**, 369
- Fabian, A. C., Johnstone, R. M., Sanders, J. S., et al. 2008, *Natur*, **454**, 968
- Fabian, A. C., & Sanders, J. S. 2006, in *ESO Astrophysics Symp.*, ed. H. Böhringer (Berlin: Springer)
- Fabian, A. C., Sanders, J. S., Crawford, C. S., et al. 2003, *MNRAS*, **344**, L48
- Fabian, A. C., Sanders, J. S., Etori, S., et al. 2000, *MNRAS*, **318**, L65
- Fabian, A. C., Sanders, J. S., Williams, R. J. R., et al. 2011, *MNRAS*, **417**, 172
- Fasano, G., & Franceschini, A. 1987, *MNRAS*, **225**, 155
- Ferland, G. J., Fabian, A. C., Hatch, N. A., et al. 2009, *MNRAS*, **392**, 1475
- Garn, T., & Best, P. N. 2010, *MNRAS*, **409**, 421
- Gaspari, M., Ruszkowski, M., & Oh, S. P. 2013, *MNRAS*, **432**, 3401
- Gendron-Marsolais, M., Hlavacek-Larrondo, J., Martin, T. B., et al. 2018, *MNRAS*, **479**, L28
- Harris, C. R., Millman, K. J., van der Walt, S. J., et al. 2020, *Natur*, **585**, 357
- Hatch, N. A., Crawford, C. S., Johnstone, R. M., & Fabian, A. C. 2006, *MNRAS*, **367**, 433
- Heckman, T. M., Baum, S. A., van Breugel, W. J. M., & McCarthy, P. 1989, *ApJ*, **338**, 48
- Hitomi Collaboration, Aharonian, F., Akamatsu, H., et al. 2016, *Natur*, **535**, 117
- Hitomi Collaboration, Aharonian, F., Akamatsu, H., et al. 2018, *PASJ*, **70**, 13
- Hunter, J. D. 2007, *CSE*, **9**, 90
- Johnstone, R. M., & Fabian, A. C. 1988, *MNRAS*, **233**, 581
- Joye, W. A., & Mandel, E. 2003, in *ASP Conf. Ser. 295, Astronomical Data Analysis Software and Systems XII*, ed. H. E. Payne, R. I. Jedrzejewski, & R. N. Hook (San Francisco, CA: ASP), 489
- Kauffmann, G., Heckman, T. M., Tremonti, C., et al. 2003, *MNRAS*, **346**, 1055
- Kent, S. M., & Sargent, W. L. W. 1979, *ApJ*, **230**, 667
- Kewley, L., Heisler, C., & Dopita, M. 2001, *ApJS*, **132**, 37
- Kewley, L. J., Groves, B., Kauffmann, G., & Heckman, T. 2006, *MNRAS*, **372**, 961
- Li, Y., Gendron-Marsolais, M.-L., Zhuravleva, I., et al. 2020, *ApJ*, **889**, L1
- Li, Z., 2023 ndtest, <https://github.com/syrte/ndtest>
- Lim, J., Ao, Y., & Dinh-V-Trung 2008, *ApJ*, **672**, 252
- Lynds, R. 1970, *ApJL*, **159**, L151
- Macquart, J.-P., Prochaska, J. X., McQuinn, M., et al. 2020, *Natur*, **581**, 391
- Marrone, D. P., Smith, G. P., Okabe, N., et al. 2012, *ApJ*, **754**, 119
- Martin, T., & Drissen, L. 2017, arXiv:1706.03230
- Martin, T. B., Prunet, S., & Drissen, L. 2016, *MNRAS*, **463**, 4223
- McDonald, M., Veilleux, S., & Rupke, D. S. N. 2011, *ApJ*, **746**, 153
- McNamara, B. R., Russell, H. R., Nulsen, P. E. J., et al. 2014, *ApJ*, **785**, 44
- McNamara, B. R., Russell, H. R., Nulsen, P. E. J., et al. 2016, *ApJ*, **830**, 79
- Minkowski, R. 1959, in *IAU Symp. 9* (Cambridge: Cambridge Univ. Press), 315
- Mittal, R., Oonk, J. B. R., Ferland, G. J., et al. 2012, *MNRAS*, **426**, 2957
- Mushotzky, R. F., Holt, S. S., Boldt, E. A., Serlemitsos, P. J., & Smith, B. W. 1981, *ApJ*, **244**, L47
- Nagai, H. 2019, in *ALMA2019: Science Results and Cross-Facility Synergies* Oh, K., Ueda, Y., Akiyama, M., et al. 2019, *ApJ*, **880**, 112
- Osterbrock, D. E. 1981, *ApJ*, **249**, 462
- Peacock, J. A. 1983, *MNRAS*, **202**, 615
- Pizzolato, F., & Soker, N. 2005, *ApJ*, **632**, 821
- Rhea, C., Hlavacek-Larrondo, J., Rousseau-Nepton, L., & Prunet, S. 2021a, *RNAAS*, **5**, 276
- Rhea, C., Hlavacek-Larrondo, J., Rousseau-Nepton, L., Vigneron, B., & Guité, L.-S. 2021b, *RNAAS*, **5**, 208
- Rhea, C. L., 2020 X-tra Astronomy Tools, <https://osf.io/vwcks/>
- Rhea, C. L., Rousseau-Nepton, L., Covington, J., et al. 2021c, crhea93/LUCI: Luci Updates, Zenodo, doi:10.5281/zenodo.5730149
- Rhea, C., Rousseau-Nepton, L., Prunet, S., Hlavacek-Larrondo, J., & Fabbro, S. 2020, *ApJ*, **901**, 152
- Riffel, R. A., Storchi-Bergmann, T., Zakamska, N. L., & Riffel, R. 2020, *MNRAS*, **496**, 4857
- Rousseau-Nepton, L., Martin, R. P., Robert, C., et al. 2019, *MNRAS*, **489**, 5530
- Rubin, V. C., Ford, W. K., Jr, Peterson, C. J., & Oort, J. H. 1977, *ApJ*, **211**, 693
- Sabra, B. M., Shields, J. C., & Filippenko, A. V. 2000, *ApJ*, **545**, 157
- Salomé, P., Combes, F., Revaz, Y., et al. 2008, *A&A*, **484**, 317
- Sanders, J. S., Fabian, A. C., Allen, S. W., & Schmidt, R. W. 2004, *MNRAS*, **349**, 952
- Scharwächter, J., McGregor, P. J., Dopita, M. A., & Beck, T. L. 2013, *MNRAS*, **429**, 2315
- Schmidt, R. W., Fabian, A. C., & Sanders, J. S. 2002, *MNRAS*, **337**, 71
- Stasińska, G., Fernandes, R. C., Mateus, A., Sodré, L., & Asari, N. V. 2006, *MNRAS*, **371**, 972
- Steidel, C. C., Erb, D. K., Shapley, A. E., et al. 2010, *ApJ*, **717**, 289
- Suresh, J., Bird, S., Vogelsberger, M., et al. 2015, *MNRAS*, **448**, 895
- Tremblay, G. R., Combes, F., Oonk, J. B. R., et al. 2018, *ApJ*, **865**, 13
- Tumlinson, J., Peebles, M. S., & Werk, J. K. 2017, *ARA&A*, **55**, 389
- Vale Asari, N., Wild, V., de Amorim, A. L., et al. 2020, *MNRAS*, **498**, 4205
- Veilleux, S., & Osterbrock, D. E. 1987, *ApJS*, **63**, 295
- Vigneron, B., Hlavacek-Larrondo, J., Rhea, C. L., et al. 2024, *ApJ*, **962**, 96
- Virtanen, P., Gommers, R., Oliphant, T. E., et al. 2020, *NatMe*, **17**, 261
- Voit, G. M., Bryan, G. L., O'Shea, B. W., & Donahue, M. 2015, *ApJ*, **808**, L30
- Werner, N., Oonk, J. B. R., Sun, M., et al. 2014, *MNRAS*, **439**, 2291
- Werner, N., Simionescu, A., Million, E. T., et al. 2010, *MNRAS*, **407**, 2063
- Wilman, R. J., Edge, A. C., & Johnstone, R. M. 2005, *MNRAS*, **359**, 755
- Wright, E. L. 2006, *PASP*, **118**, 1711
- Yu, A. P.-Y., Lim, J., Ohyama, Y., Chan, J. C.-C., & Broadhurst, T. 2015, *ApJ*, **814**, 101
- Zhu, G., & Ménard, B. 2013, *ApJ*, **773**, 16